Small Core Axial Compressors for High Efficiency Jet Aircraft

by

Austin Graf DiOrio

B.S. in Mechanical Engineering
Johns Hopkins University (2010)

Submitted to the Department of Aeronautics and Astronautics
in partial fulfillment of the requirements for the degree of

Master of Science

at the

MASSACHUSETTS INSTITUTE OF TECHNOLOGY

September 2012

Author . . . .
Department of Aeronautics and Astronautics
August 23, 2012

Certified by . . . .
Edward M. Greitzer
H.N. Slater Professor of Aeronautics and Astronautics
Thesis Supervisor

Certified by . . . .
Choon Sooi Tan
Senior Research Engineer
Thesis Supervisor

Accepted by . . . .
Eytan H. Modiano
Professor of Aeronautics and Astronautics
Chair, Graduate Program Committee

Small Core Axial Compressors for High Efficiency Jet Aircraft

by

Austin Graf DiOrio

Submitted to the Department of Aeronautics and Astronautics
on August 23, 2012, in partial fulfillment of the
requirements for the degree of
Master of Science

Abstract

This thesis quantifies mechanisms that limit efficiency in small core axial compressors, defined here as compressor exit corrected flow between 1.5 and 3.0 lbm/s. The first part of the thesis describes why a small engine core with high overall pressure ratio (OPR) is desirable for an efficient aircraft and shows that fuel burn can be reduced by up to 17% compared to current engines. The second part examines two specific effects: Reynolds number and tip clearance. At a core size of 1.5 lbm/s, Reynolds number may be as low as 160,000, resulting in reductions in stage efficiency up to 1.9% for blades designed for high Reynolds number flow. The calculations carried out indicate that blades optimized for this Reynolds number can increase stage efficiency by up to 1.6%. For small core compressors, non-dimensional tip clearances are increased, and it is estimated that tip clearances can be up to 4.5% clearance-to-span ratio at the last stage of a 1.5 lbm/s high pressure compressor. The efficiency penalty due to tip clearance is assessed computationally and a 1.6% decrease in polytropic efficiency is found for a 1% increase in gap-to-span ratio. At the above clearance, these efficiency penalties increase aircraft mission fuel burn by 3.4%, if current design guidelines are employed. This penalty, however, may be reduced to 0.4% if optimized blades and a smaller compressor radius than implied by geometric scaling, which allows reduced non-dimensional clearance, are implemented. Based on the results, it is suggested that experiments and computations should be directed at assessing: (i) the effects of clearance at values representative of these core sizes, and (ii) the effect of size on the ability to achieve a specific blade geometry and thus the impact on loss.

Thesis Supervisor: Edward M. Greitzer
Title: H.N. Slater Professor of Aeronautics and Astronautics

Thesis Supervisor: Choon Sooi Tan
Title: Senior Research Engineer

Acknowledgments

I would like to thank Professor Greitzer and Dr. Tan for their guidance and support in formulating this thesis. They provided a wealth of technical expertise when needed. More importantly, they created an open learning environment in which I could think and discover independently.

I am especially grateful for the Aurora Flight Sciences Fellowship awarded to me my first year of graduate school. This fellowship provided me with the necessary support and freedom to get a solid start on my degree. I thank Aurora Flight Sciences for funding this fellowship and the MIT Department of Aeronautics and Astronautics for bestowing this award to me.

I am thankful for the NASA N+3 project which has provided financial support for this project. I would like to thank those on the MIT N+3 team for their help and guidance including Professor Drela, Arthur Huang, David Hall, and Nathan Fitzgerald from Aurora Flight Sciences.

I would also like to thank Pratt and Whitney for sharing their expertise on compressor and engine design. I would particularly like to thank Wes Lord, Andrew Murphy, Gabriel Suciu, Lisa Brilliant, and Sean Nolan for their time and intellectual contributions to this project and Jayant Sabnis for his overall support of the project. They were able to share a knowledge base much different that that found here at the Gas Turbine Lab.

I want to thank all of the members of the Gas Turbine Laboratory as almost all of you have contributed in one way or another to the formulation of this thesis. Thank you for being able to answer my questions when needed and providing a wonderful environment in which to work.

Lastly, I want to thank my family for always supporting me in the many endeavors of my life. The have always stood beside me, no matter what path I have taken. Their love and care for me never ceases to amaze me.

Contents

List of Figures

List of Tables

Nomenclature

Symbols

a speed of sound

A area

AR aspect ratio

C blade chord

C_d dissipation coefficient

c_p specific heat at constant pressure

c_y coefficient of moment

D diameter

F force (thrust)

g blade stagger spacing

GR growth

h enthalpy

M Mach number

$\dot{m}$ mass flow

NO_x nitrogen oxide

p blade pitch

P pressure

R ideal gas constant

Re Reynolds number

s entropy

S blade span

T temperature

Tu turbulence level

u velocity

U blade velocity

V velocity

w, W relative velocity

$\dot{W}$ rate of work (power)

α relative flow angle, local blade camber angle

γ ratio of specific heats

$\delta*$ boundary layer displacement thickness

ε physical tip gap

Δ change

η efficiency

θ deflection angle

ν kinematic viscosity

π pressure ratio

ρ density

ξ incidence angle

σ solidity

υ tangential force thickness

Σ sum

ψ' stage pressure rise coefficient

χ blade stagger angle

ω stagnation pressure loss coefficient

ϕ flow coefficient

Ω angular rotation

Subscripts

1 blade row entrance

2 blade row exit, engine inlet face

3 compressor outlet

4 turbine inlet

5 turbine outlet

air air

$adia$ adiabatic (efficiency)

b bypass

c core

$comp$ compressor

f fuel

$isen$ isentropic (efficiency)

j jet

n net

o overall

p blade pressure side

s blade suction side

t tip

th thermal (efficiency)

$turb$ turbine

$0, t$ stagnation quantity

θ tangential direction

∞ free-stream condition

Superscripts

rel relative

$\sim$ pertaining to free-stream profiles

Abbreviations

BL boundary layer

BLI boundary layer ingestion/ingesting

CAEP committee on aviation environmental protection

CFD computational fluid dynamics

DTE divergent trailing edge

EPNL effective perceived noise level

FPR fan pressure ratio

HPC high pressure compressor

HPT high pressure turbine

LE leading edge

LPC low pressure compressor

LCV lower caloric value (fuel energy)

LP low pressure

LPT low pressure turbine

LSAC low speed axial-flow compressor

LTO low temperature oxidation

OPR overall pressure ratio

PR pressure ratio

PFEI payload fuel efficiency intensity

RANS Reynolds-averaged Navier-Stokes

TE trailing edge

Chapter 1

Introduction

Reducing fuel consumption and noise generation are high priorities in the aviation industry today. Aircraft propulsion systems can be altered to reduce fuel burn and noise by increasing overall pressure ratio (OPR) and reducing fan pressure ratio (FPR). These changes to the thermodynamic cycle of a turbofan engine are accompanied by reductions in the size of the core and possibly higher losses in the compressor system. In this thesis, we investigate mechanisms that can lead to decreased efficiency (compared to large core machines) in a high pressure ratio, small core axial compressor (overall pressure ratio 50+, exit corrected flow 1.5 lbm/s) and propose some conceptual approaches to mitigating these losses.

1.1 Small Core, High Efficiency Engine Defined

1.1.1 Small Core

The core of a jet engine can be defined for this thesis as the high pressure compressor, combustor, and high pressure turbine. Figure 1-1 shows a cross-section of a two-spool, high bypass ratio, turbofan engine with the red box indicating the engine core. The engine core generates high temperature, high pressure gas that can be used to drive a turbine to produce useful work. For the case of interest here, this includes driving a large diameter fan.

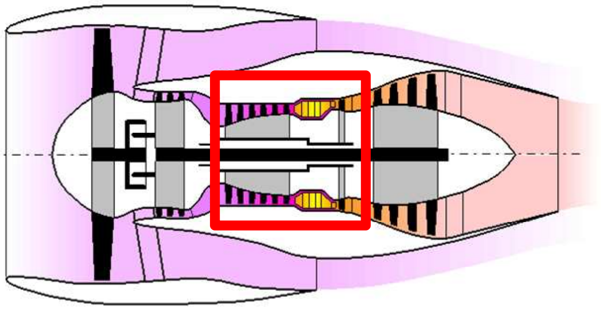

Figure 1-1: Cross section of a turbofan engine. The engine core is identified with a red box.

The size of a core is typically defined by the corrected flow at the high pressure compressor (HPC) exit. The corrected mass flow per unit area is a non-dimensional parameter that is a function of the Mach number.

$$f(M, \gamma) = \frac{\dot{m}\sqrt{R T_t}}{A P_t} \tag{1.1}$$

Equation 1.1 can be rearranged to give an expression for the physical area of a compressor as,

$$A = \underbrace{\frac{1}{f(M, \gamma)}}_{(1)} \underbrace{\left(\frac{\dot{m}\sqrt{R T_t}}{P_t} \right)}_{(2)} \tag{1.2}$$

Term (1) in Equation 1.2, the reciprocal of the corrected mass flow per unit area, is a function of Mach number and specific heat ratio γ. This value does not vary greatly over a range of engines as the combustor tends to set the exit Mach number and term (2) in Equation 1.2 is related to corrected flow

$$Corrected\ Flow = \frac{\dot{m}\sqrt{T_t / T_{t\,ref}}}{P_t / P_{t\,ref}} \tag{1.3}$$

If the exit Mach number can be considered constant, the physical area of the compressor is proportional to the corrected flow. Corrected flow will be used throughout this thesis to quantify core size.

1.1.2 High Efficiency

Thermal efficiency for the core is defined as the net work produced divided by the energy extracted from the fuel. In terms of power,

$$\eta_{th} = \frac{\dot{W}_{net}}{m_f \dot{L}CV} \tag{1.4}$$

The core power is defined by (with π as the pressure ratio)

$$\dot{W}_{net} = \dot{m}_{air} c_p T_{02} \left(\eta_{adia,turb} \frac{T_{04}}{T_{02}} \left(1 - 1/\pi^{(\gamma-1)/\gamma}\right) - \frac{\left(\pi^{(\gamma-1)/\gamma} - 1\right)}{\eta_{adia,comp}} \right) \tag{1.5}$$

From Equations 1.4 and 1.5, to increase thermal efficiency, one can increase the adiabatic efficiency of the compressor and/or increase the overall pressure ratio (OPR) of the engine.

To achieve high thermal efficiency, high component efficiency and high OPR are thus necessary. Thus, the three characteristics of a high efficiency small core engine defined here are:

- Low corrected mass flow (HPC exit corrected flow between 1.5 lbm/s and 3 lbm/s in this thesis)
- High component efficiency (compressor polytropic efficiency desired to be greater than 90%)
- High overall pressure ratio (OPR greater than 50)

1.2 Motivation for Study: The D8.6 Aircraft

As fuel prices rise, environmental regulations tighten, and noise restrictions go into effect, there is a desire for jet engines to have lower fuel consumption and lower noise generation. This need is reflected in NASA's N+3 initiative which is defining the the conceptual development of aircraft for the 2035 time frame. The fuel burn, noise, and emission requirements of NASA's N+3 initiative are summarized in Table 1.1.

Metric	N+3 Goal
Fuel Burn	60% reduction compared to current aircraft
Noise	71 EPNdB below stage 4
LTO NOx	80% below CAEP 6

Table 1.1: NASA N+3 goals as of June 2011 [16].

MIT has developed a conceptual aircraft to meet the requirements set forth by NASA. This aircraft, known as the D8.6, is designed to fill a role similar to that of a B737 or A320 class aircraft in the 2035 time frame. The D8.6 tube and wing aircraft concept includes a number of unique features that reduce weight and drag including a lifting body, high aspect ratio wings, composite materials, and boundary layer ingestion (BLI).

Figure 1-2: Artist's rendering of the D8.6 aircraft.

The aircraft design was created primarily using the Transport Aircraft System OPTimization (TASOPT) code [7]. This first principles code allows the user to design and optimize the mission, airframe, and propulsion system of a tube and wing aircraft. This code includes an engine cycle model along with empirical relationships to estimate the drag and weight of a specific engine design. The D8.6 engine cycle is defined in Table 1.2 and compared to the CFM56-7B26, an engine for the B737-800 aircraft.

	CFM56-7B26	D8.6 Engine
Thrust	26,300 lbf	13,000 lbf
OPR	33	50
BPR	5.1	20
HPC Exit Corrected Flow	7 lbm/s	1.5 lbm/s

Table 1.2: Engine cycle comparison between a B737-800 and D8.6 [10, 12].

Table 1.2 illustrates the primary differences between a present day engine cycle, and the D8.6 engine cycle. The low thrust value, high OPR, and high BPR combine to reduce HPC exit corrected flow to 1.5 lbm/s, approximately 20% the amount of the CFM56-7B26 and from the discussion in Section 1.1, the area of the D8.6 core will be roughly 20% the size that for a CFM56-7B26.

1.3 Challenges of a High Efficiency Small Core

1.3.1 High Temperature at High OPR

As the physical size of compressor blades reduces, engine companies have tended to use centrifugal compressors, which achieve higher polytropic efficiency than small axial blades, in lieu of rear axial stages. However, as the overall pressure ratio of the engine increases, the air temperature at the rear of the HPC can become an issue for a centrifugal compressor. With polytropic efficiencies of 90% and an OPR of 50, the temperature at the rear of the HPC is 790^{o}C during takeoff on a 35^{o}C day. This high temperature combined with the high rotation rate of the centrifugal rotor leads to large stresses on the disk and for this reason, centrifugal aeroengines do not OPRs above 30. This thesis thus focuses on axial compressors to achieve the OPR levels sought.

1.3.2 Low Polytropic Efficiency

The difficulty with an all-axial design is maintaining high polytropic efficiencies at small geometric sizes and the overarching focus of this research is to define the mechanisms that limit efficiency in small core axial compressors.

The decrease in polytropic efficiency for a physically small axial compressor is expected for three reasons.

1. Low Reynolds number effects.

2. Large tip clearances.

3. Geometry limitations due to manufacturing.

Low Reynolds Number Effects

The first mechanism of inefficiency we discuss is the effect of low Reynolds number; as blades decrease in chord length, chord Reynolds number decreases. As shown in Appendix A, small core engines can have Reynolds numbers as low as 160,000.

There exists previous work on the issue of low Reynolds numbers in compressors. Roberts performed cascade experiments and found loss coefficients increased by more than 50% from Re = 300,000 to Re = 100,000 [24]. Schaffler carried out an experimental investigation of entire high pressure compressors. Although dependent on the specific machine tested, Schaffler found a polytropic efficiency decrease of 3-6% for operation at Re = 100,000 compared to Re =1,000,000 [26]. It is important to note, however, that such experiments were conducted for blades and compressors not designed for low Reynolds number flow. A substantial portion of this thesis is devoted to developing estimates of the efficiency benefit associated with blades optimized for low Reynolds number flow. We examine this in Chapter 3.

Large Tip Clearances

Tip clearance losses have been investigated extensively. Freeman found a 2.5% decrease in adiabatic efficiency as the tip clearance increased from 0.9% to 3.4% [9]. Most research has dealt with clearances below 4% clearance-to-span ratio because of the high efficiency penalty above 4%. As compressors decrease in physical size, however, there is a limit on how small a gap can be maintained between rotor and shroud having to do with manufacturing limitations, as well as operational constraints. The non-dimensional clearance-to-span ratio is estimated to be up to 4.5% in a small core compressor, as discussed in Chapter 4.

Geometric Limitations Due to Manufacturing

As compressor size decreases, manufacturing limitations and tolerances become more prominent. The minimum leading edge radius and trailing edge thickness of a compressor blade are set by material strengths and the machinability of metals. For small core compressor blades, blade shape may be significantly altered, in terms of losses, from the aerodynamic optimum due to these limitations. Blade profile losses can thus increase as the physical size of blades decrease. Fillets, seals, and gaps also become larger in a non-dimensional sense in a small core compressor. This thesis will not investigate the effects of manufacturing other than tip clearances, but future work on small core compressors should examine the important role of manufacturing and tolerances.

1.4 Intellectual Contributions

The contributions of this thesis include:

1. Determination of the impact of engine cycle on aircraft fuel burn and core size.
2. Quantification of the efficiency penalty of low Reynolds number operation of a compressor stage. This includes blade optimization to reduce the losses of compressor airfoils in low Reynolds number flow and assessment of potential efficiency improvement.
3. Estimation of the relationship between non-dimensional tip clearance and polytropic efficiency in an isolated rotor row using a simple computational model of an embedded rotor.
4. Estimation of HPC polytropic efficiency for different core sizes, compressor configurations, and tip clearance scaling.
5. Calculation of aircraft fuel burn penalty due to inefficiencies associated with small core HPCs.

1.5 Thesis Outline

Chapter 2 provides background on the desirability of small core engines. The chapter illustrates the benefits of increasing overall pressure ratio (OPR) and decreasing fan pressure ratio (FPR) in a turbofan and how these changes lead to a smaller core. In Chapter 3, small core configurations are examined to assess Reynolds number effects and the potential of blade optimization to minimize losses. In Chapter 4 we investigate tip clearance losses and how compressor efficiency decreases with increasing tip clearance in an embedded stage. Chapter 5 uses the work of the preceding chapters in determining the effects of decreasing compressor size on aircraft fuel burn. Chapter 6 concludes with a summary and discussion of potential future work.

Chapter 2

Small Core Desirability

This chapter investigates cycle changes that can lead to increased efficiency in jet engines. Arguments are presented to illustrate why small core jet engines are desirable for decreased fuel burn in future civil jet engines.

2.1 Cycle Modifications to Decrease Fuel Burn

2.1.1 Performance Metrics

A metric directly related to fuel burn is overall efficiency of the engine, defined as useful work over fuel energy.

$$\eta_{overall} = \frac{F_N\, V_\infty}{\dot{m}_f\, LCV} \tag{2.1}$$

The overall efficiency is the product of thermal and propulsive efficiency.

$$\eta_{overall} = \eta_{thermal}\eta_{propulsive} \tag{2.2}$$

Thermal efficiency was introduced in Equation 1.4. Propulsive efficiency is defined as the thrust power of the aircraft divided by the power of the jet.

$$\eta_{propulsive} = \frac{V\left[(m_{air} + m_f)V_j - m_{air}V\right]}{\frac{1}{2}\left[(m_{air} + m_f)V_j^2 - m_{air}V^2\right]} \tag{2.3}$$

Propulsive efficiency tends to unity as the jet velocity approaches the speed of the aircraft, so lower fan pressure ratio (FPR) leads to higher propulsive efficiency.

A second parameter used to describe the efficiency of a jet engine is the Thrust Specific Fuel Consumption (TSFC). The units of TSFC are mass flow per unit force (e.g. kg/N-s). TSFC is useful as it allows different sized engines to be compared.

$$TSFC = \frac{\dot{m}_f}{F_N} \tag{2.4}$$

The overall efficiency can be written in terms of TSFC.

$$\eta_{overall} = \frac{1}{TSFC}\frac{V_\infty}{LCV} \tag{2.5}$$

2.1.2 Overall Pressure Ratio Increase

For component polytropic efficiencies greater than 90%, increasing the overall pressure ratio increases the thermal efficiency of a jet engine for all practical OPR values. The root of this increase is found in Equations 1.4 and 1.5 and Figure 2-1 shows the effect of OPR on overall efficiency for $\eta_{poly} = 0.90$.

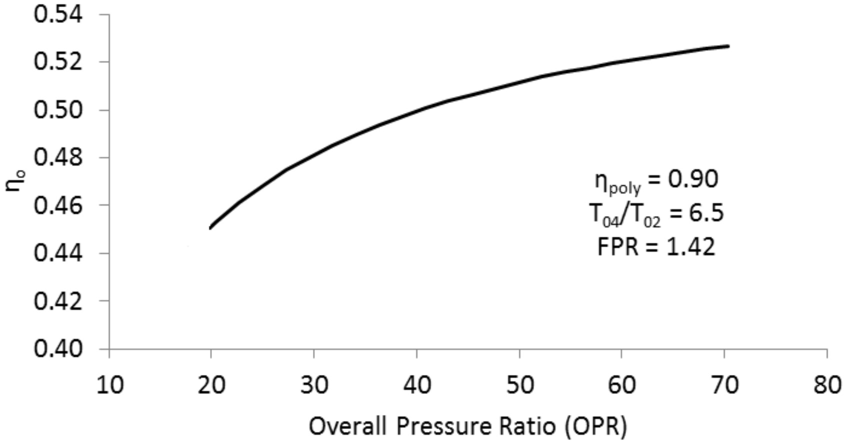

Figure 2-1: Overall efficiency versus OPR, no turbine cooling.

Figure 2-1 gives overall pressure ratio on the x-axis and overall efficiency on the y-axis. The OPR range was selected to span a current small core engine (PW308B engine, OPR 27) and the D8.6 engine (OPR 50) [10,12]. The PW308B engine is in the same thrust class as the D8.6 engine and it will be used in a comparison with the D8.6 engine later in this chapter. A two-spool turbofan cycle is also assumed, as that is the D8.6 engine cycle. The polytropic efficiency, temperature ratio, and fan pressure ratio are all also based on the D8.6 cycle [10]. For simplicity, pressure losses between engine components were neglected, the core nozzle velocity was assumed equal to the bypass nozzle velocity, and turbine cooling was not included.

2.1.3 Fan Pressure Ratio Decrease

Decreasing fuel burn is also accomplished by decreasing the fan pressure ratio (FPR) of the engine and hence the exit jet velocity. From Equation 2.3, as jet velocity decreases, propulsive efficiency increases. Figure 2-2 shows overall efficiency versus FPR illustrating the increase in efficiency with decreasing FPR. The x-axis of Figure 2-2 is FPR and the y-axis is overall efficiency, and the figure was generated using the same assumptions as Figure 2-1. The range of FPR spans the PW308B (FPR 1.7) and the D8.6 engine (FPR 1.42) [10, 12].

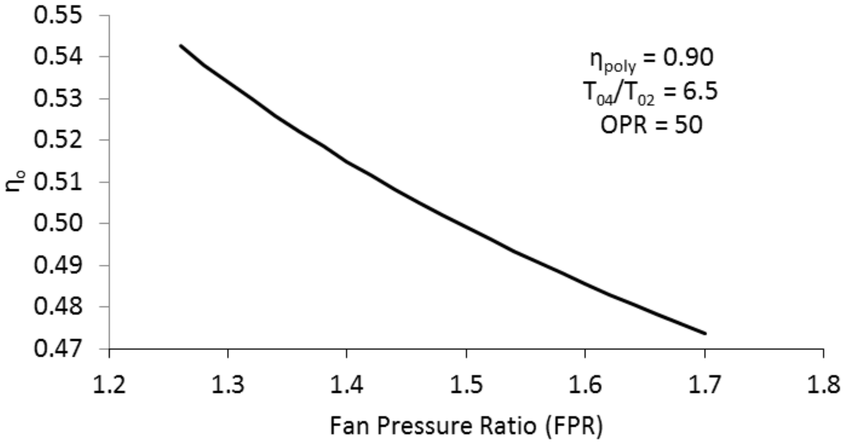

Figure 2-2: Overall efficiency versus FPR.

A second motivation for decreasing the fan pressure ratio of a jet engine is that the noise produced by an engine decreases with FPR. Guynn quantified the engine noise variation with FPR and Figure 2-3 shows the results [14]. The EPNL level is seen to decrease by 15 dB if the FPR is decreased from 1.7 to 1.4.

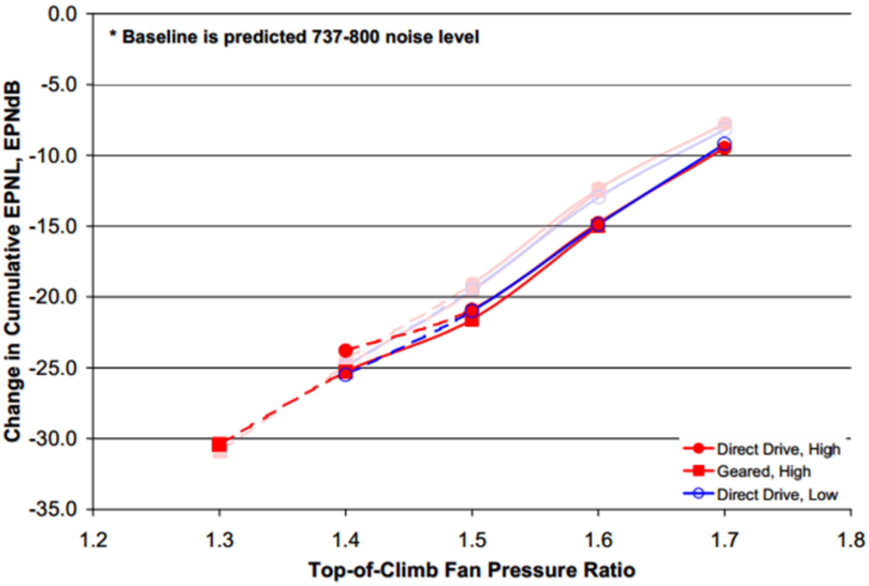

Figure 2-3: Noise versus FPR from Guynn et. al. [14].

2.1.4 Implication on Core Size

To demonstrate the effects of OPR and FPR on core size, the program GasTurb, which calculates parameters for any gas turbine thermodynamic cycle, was employed. Figure 2-4 illustrates the variation in HPC corrected flow with OPR and FPR. The the x-axis is overall pressure ratio and the y-axis is HPC exit corrected flow (i.e core size). Each line represents a different FPR. The range of OPR and FPR was selected to include the PW308B and D8.6 values, as was done in Figures 2-1 and 2-2. The thrust, temperature ratio, and component efficiencies were held constant at the D8.6 cruise values [10].

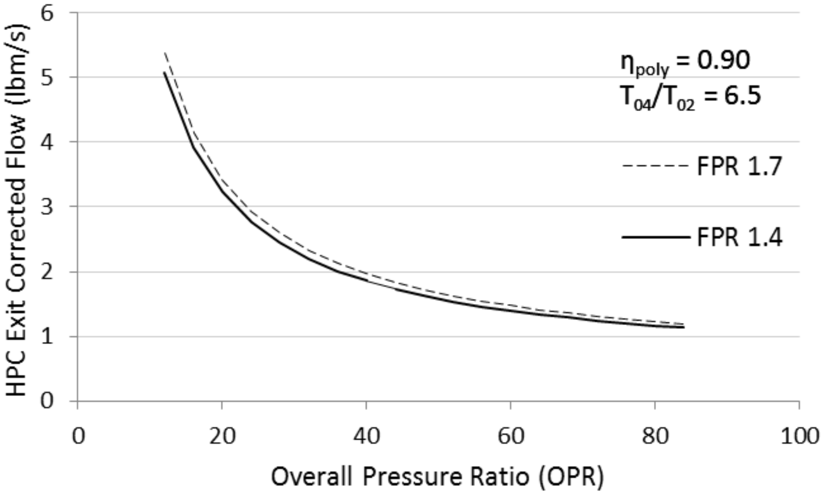

Figure 2-4: HPC corrected flow versus OPR for different FPRs. Thrust held constant at the D8.6 value (see Table 1.2).

Figure 2-4 shows that as OPR increases, HPC exit corrected flow decreases. A higher OPR implies a higher pressure at the rear of the HPC, which means a lower corrected flow as evident from Equation 1.3. A decrease in FPR also decreases core size, but through a different mechanism. A lower FPR results in a higher propulsive efficiency and thus higher overall efficiency, implying that less power needs to be produced by the core, reducing the needed physical mass flow.

2.2 Core Size Impact on Fuel Burn

The arguments for decreasing compressor size have so far been made from a thermodynamic viewpoint. We now take a systems approach (include the entire aircraft and mission) to illustrate the impact of core size on fuel burn, the metric of primary concern for the N+3 project.

Increasing OPR and decreasing FPR both improve cycle efficiency, but these changes can have adverse effects on aircraft performance. For the same thrust, a lower FPR implies a higher BPR, leading to a larger engine and hence more drag. A higher OPR also indicates a need for more compressor stages, adding weight.

To investigate the effect of cycle design on aircraft performance, the TASOPT code, a software tool that optimizes the design of a commercial aircraft, was used [7]. Aircraft parameters such as wing aspect ratio, fuselage fineness, engine cycle definition, and nacelle drag are included in the analysis.

In phase I of the N+3 project, assumptions of component efficiencies were made for the D8.6 aircraft [10]. Table 2.1 lists component efficiency assumptions.

Component	Polytropic Efficiency
Fan	95.1%
LPC	93.0%
HPC	90.0%
HPT	92.5%
LPT	93.0%

Table 2.1: Assumed efficiencies for the D8.6 aircraft [10].

As shown in Figure 2-4, OPR is a factor for core size and fuel burn has been calculated at different OPR values. The fuel burn metric used was Payload Fuel Efficiency Intensity (PFEI), the ratio of fuel energy burned divided by payload times range. PFEI is not linked to any specific fuel, broadening its applicability. A baseline OPR value of 30 was selected as a reference for comparison with current engines of the same thrust class (e.g. PW308B) [12].

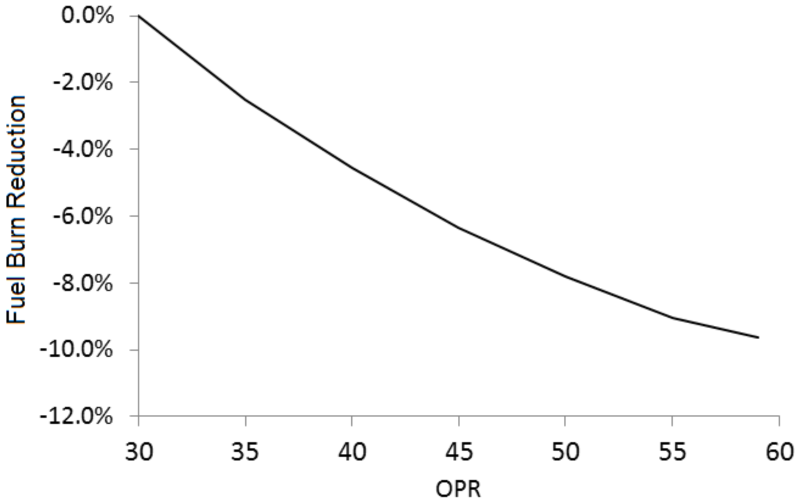

Figure 2-5: PFEI fuel burn savings versus OPR. Calculations assume efficiencies as in Table 2.1. FPR is 1.42, T_{04}/T_{02} is 6.5, and thrust is held constant to the D8.6 value (see Table 1.2).

Figure 2-5 illustrates the benefit of a high OPR jet engine. The x-axis of Figure 2-5 is OPR and the y-axis is percent reduction in fuel burn. Increasing OPR from 30 to 50 decreases fuel burn by 7.8%. This increase in OPR leads to a decrease in core size from 2.32 lbm/s to 1.58 lbm/s, or 31.9%, for the D8.6 thrust value.

The benefits of a small core become more apparent when comparing the D8.6 cycle with that of the PW308B. To make the comparison on the basis of cycle alone, the component efficiencies were assumed the same for each. The cycle parameters for both engines are listed in Table 2.2. Optimizing the aircraft for each engine using TASOPT, we find that fuel burn is reduced by 17.0% and core size by 50.5% for the D8.6 aircraft.

	PW308B	D8.6
OPR	27	50
FPR	1.68	1.42

Table 2.2: PW308B and D8.6 engine cycle parameters.

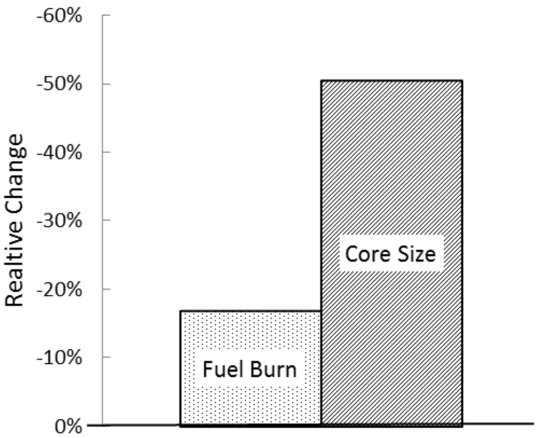

Figure 2-6: Decrease in fuel burn and core size for the D8.6 aircraft compared to an optimized aircraft with a PW308B engine cycle.

Figure 2-6 presents the decrease in fuel burn and core size for the D8.6 compared to an optimized aircraft with a PW308B cycle. There is a 17.0% decrease in fuel from the lower FPR, higher OPR cycle, and the core size decreases by 50.5%, in agreement with Figure 2-4.

2.3 Acceptable Polytropic Efficiency Decrease

At this point, the connections between cycle changes (i.e. OPR and FPR) and core size and fuel burn are known. However, the adverse effect of small compressor size has not been accounted for. In this section, a performance benchmark is developed to exhibit the effect of reduction in compressor efficiency. Using a D8.6 engine with a FPR of 1.42 and efficiencies in Table 2.1, we can vary OPR and HPC polytropic efficiency to find contours of thermal efficiency.

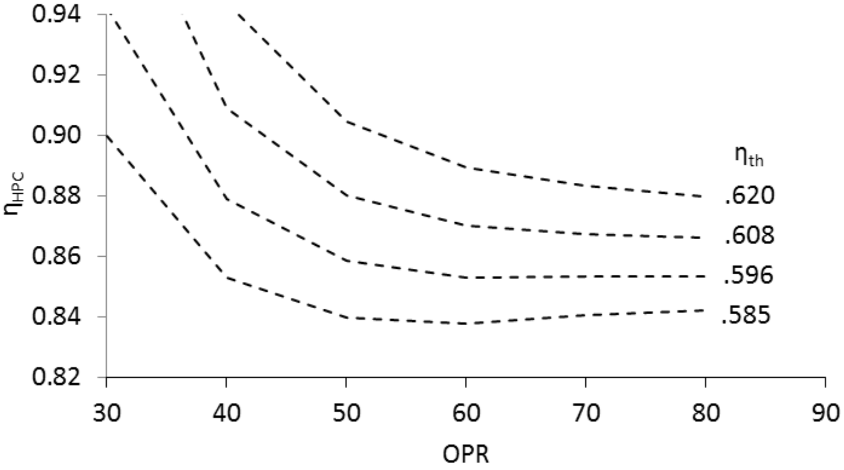

Figure 2-7: Contours of thermal efficiency for HPC polytropic efficiency and OPR. FPR is 1.42, T_{04}/T_{02} is 6.5, and thrust is held constant to the D8.6 value (see Table 1.2). Component efficiencies from Table 2.1 and turbine cooling as from Phase I [7].

The dashed lines in Figure 2-7 are contours of constant thermal efficiency so Figure 2-7 links thermal efficiency to HPC polytropic efficiency goals. The x-axis is OPR and the y-axis is the necessary HPC polytropic efficiency to achieve the overall efficiency. The lowest contour, $\eta_{th} = 0.585$, is the thermal efficiency achieved at a reference case of OPR 30 and $\eta_{HPC} = 0.90$. The other contours represent 2% increases in thermal efficiency. Figure 2-7 demonstrates the effects of both η_{HPC} and OPR on thermal efficiency; a decrease in η_{HPC} does not mean there is necessarily a decrease in η_{th}.

2.4 Impact of Compressor Efficiency on Fuel Burn

Section 2.2 showed the benefit of a small core engine assuming that the polytropic efficiency of the compressor does not vary with size. As discussed in Section 1.3, however, polytropic efficiency is expected to decrease with core size. To understand the effect of decreased compressor efficiency on overall aircraft performance, the fuel burn was calculated as a function of HPC polytropic efficiency. For given component efficiencies in a jet engine (e.g. HPC, LPT, etc.) there is an optimal engine cycle which maximizes overall efficiency. The entire airframe can also be designed to minimize fuel burn given engine performance. TASOPT optimizes the engine cycle in addition to macroscopic aircraft design parameters.

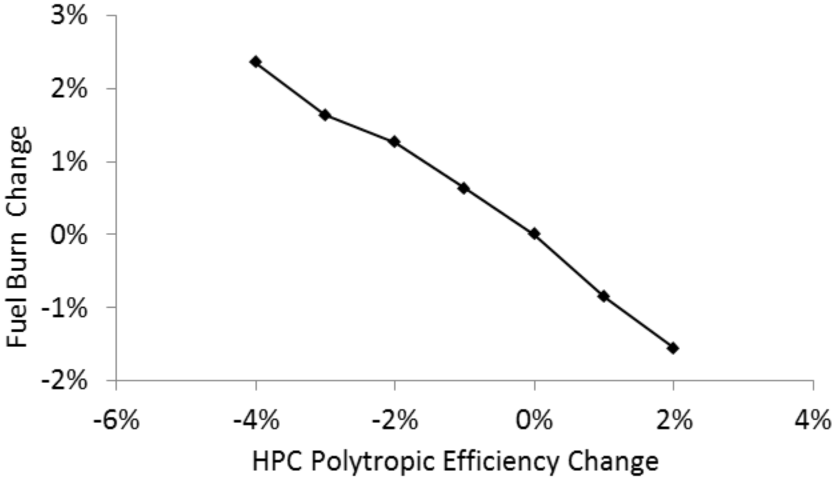

Figure 2-8: Fuel burn change as a function of HPC polytropic efficiency change. D8.6 HPC polytropic efficiency 90%. All other efficiencies defined in Table 2.1.

Figure 2-8 shows fuel burn change as a function of HPC polytropic efficiency change. The x-axis is the relative change in HPC polytropic efficiency compared to the D8.6 nominal value of 90%. The y-axis is the relative fuel burn change to the D8.6 fuel burn. If we approximate the relationship between fuel burn and efficiency to be linear, the relationship between fuel burn and efficiency is given by Equation 2.6.

$$\%\,\text{Change in fuel burn} = 0.61(\%\text{Change in HPC efficiency}) \tag{2.6}$$

A 1% change in HPC efficiency will lead to a 0.61% change in fuel burn, indicating how critical compressor efficiency is to overall aircraft performance.

Chapter 3

Reynolds Number Effects on Small Core Compressor Efficiency

A potential hurdle to developing a small core compressor is the efficiency penalty associated with operating at low Reynolds numbers. (Defined here as Reynolds numbers as low as 160,000.) This chapter describes the impact of Reynolds number on compressor efficiency and the efficiency benefits of optimized blading.

3.1 Compressor Configuration

To start we point out that blade sizes and Reynolds numbers are dependent on the compressor configuration. The configuration, in turn, is the result of many design choices, and its detailed determination is beyond the scope of the thesis. To bound the problem therefore we have considered three types of compressor configurations.

1. Pure Scale - A modern axial compressor with a hub-to-tip ratio of 0.93 at the last stage and an exit corrected flow of 6.0 lbm/s is geometrically scaled to 1.5 lbm/s corrected flow.

2. Shaft Limited - The pure scale configuration may not be mechanically feasible because the LP shaft must fit through the center of the HPC in a conventional engine design. To accommodate the LP shaft, it may be impossible to carry out

pure scaling. A “shaft limited design” was thus included in this study to account for the possibility of increased mean radius and hub-to-tip ratio because of this constraint. The mean radius for the shaft limited configuration was taken to be no smaller than an existing engine with a similar thrust, the PW308B. From a cross section provided in Jane’s Aero-Engines, the mean radius for the PW308B was found to be 0.15 meters and for the shaft limited configuration, the mean radius of the compressor will be no smaller than 0.15 meters [12].

3. Shaft Removed - Small blades present structural, manufacturing, and aerodynamic challenges to compressor design and it may be beneficial to have larger blade heights than those in the first two configurations. This can be achieved if we are able to remove the LP shaft constraint and pull in the flow path. A minimum blade height of 0.5” at 1.5 lbm/s was selected for this configuration, leading to a hub-to-tip ratio of 0.85 for the rear stage.[1] In this thesis, the shaft removed configuration thus implies a rear stage hub-to-tip ratio of 0.85.

Figure 3-1 illustrates the difference between the three different compressor configurations. The x-axis is axial distance and the y-axis is radial distance. The blade aspect ratios were assumed to be that of the E^3 compressor, as given in Table A.2. (E^3 refers to the Energy Efficient Engine initiative sponsored by NASA.) This is a nine stage HPC with the D8.6 pressure ratio of 22 [10]. A nine stage machine was selected as it gives pressure ratios approximately that of the GE90 HPC [12]. Table 3.1 is a stage by stage summary of the assumed HPC.

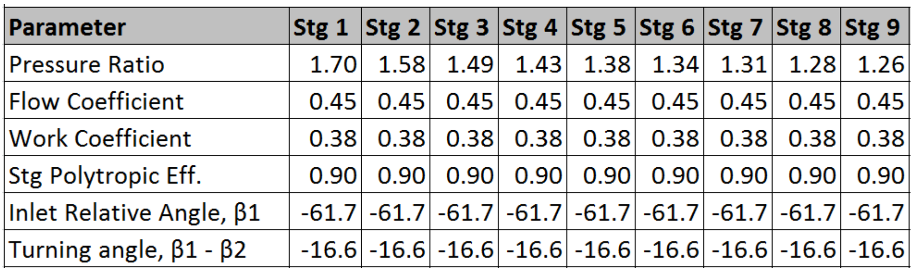

Parameter	Stg 1	Stg 2	Stg 3	Stg 4	Stg 5	Stg 6	Stg 7	Stg 8	Stg 9
Pressure Ratio	1.70	1.58	1.49	1.43	1.38	1.34	1.31	1.28	1.26
Flow Coefficient	0.45	0.45	0.45	0.45	0.45	0.45	0.45	0.45	0.45
Work Coefficient	0.38	0.38	0.38	0.38	0.38	0.38	0.38	0.38	0.38
Stg Polytropic Eff.	0.90	0.90	0.90	0.90	0.90	0.90	0.90	0.90	0.90
Inlet Relative Angle, β1	-61.7	-61.7	-61.7	-61.7	-61.7	-61.7	-61.7	-61.7	-61.7
Turning angle, β1 - β2	-16.6	-16.6	-16.6	-16.6	-16.6	-16.6	-16.6	-16.6	-16.6

Table 3.1: HPC stage by stage summary.

---

[1] Selected based on a discussion with Pratt and Whitney [1].

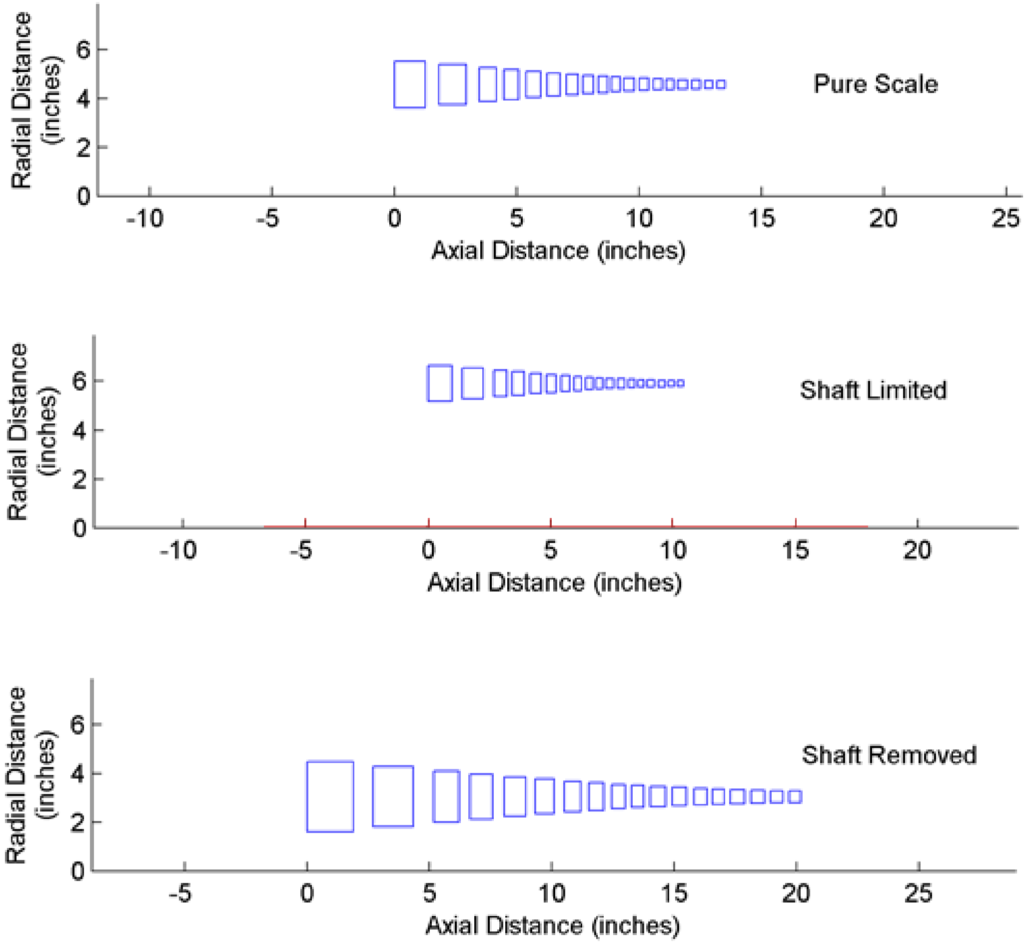

Figure 3-1: Geometries of three compressor configurations.

Table 3.2 summarizes the three different configurations for a 1.5 lbm/s machine. For each of these machines, rotor Reynolds numbers, based on the method described in Appendix A, are given in Table 3.2.

	Pure Scale	Shaft Limited	Shaft Removed
Min. Reynolds Number	206,000	160,000	309,000
Min. Blade Height (inches)	0.33	0.26	0.50
Mean Radius (inches)	4.57	5.91	3.06
Last Stage Hub-to-tip Ratio	0.93	0.96	0.85

Table 3.2: Reynolds number and geometric parameters of three compressor configurations at a core size of 1.5 lbm/s.

3.2 Reynolds Numbers In the D8.6 HPC

For the first part of this investigation, the compressor configuration was assumed to be shaft limited. This is a "worst case" assumption as it has the smallest blades and lowest Reynolds numbers. Figure 3-2 shows Reynolds number for the different compressor stages for a shaft limited configuration. The x-axis is compressor stage and the y-axis is rotor Reynolds number. Blade chord was set by assuming E^3 aspect ratios (given in Table A.2). The blading geometry was from the NASA E^3 Low Speed Research Compressor, described by Wellborn [29].

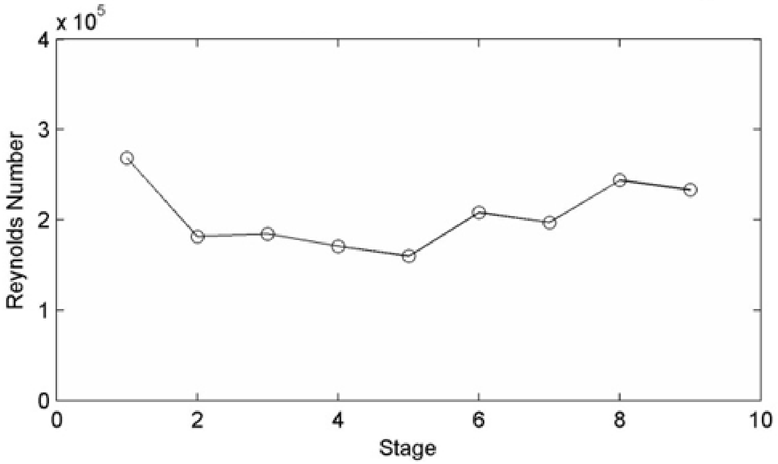

Figure 3-2: Rotor Reynolds numbers at different stages in the D8.6 axial compressor for a shaft limited configuration at a core size of 1.5 lbm/s.

One observation in Figure 3-2 is that the lowest Reynolds number value, 160,000, does not occur in the rear of the compressor where the blades are the smallest, but rather in the middle of the machine. There are two competing effects that lead to this situation. The cross sectional area of the compressor decreases since density increases leading to smaller blades. However, the kinematic viscosity also decreases through the compressor, tending to increases the Reynolds number, $Re = \frac{Vc}{\nu}$. If blade aspect ratio were constant, the result would be a decreasing Reynolds number moving from front to rear of the HPC. However, since blade aspect ratio tends to increase towards the rear of the compressor for the E^3 design, there is not a monotonic trend in Reynolds number.

3.3 Mechanisms for Increased Loss at Low Reynolds Number

Figure 3-3 below illustrates three regimes of blade Reynolds number operation defined by Schaffler [26].

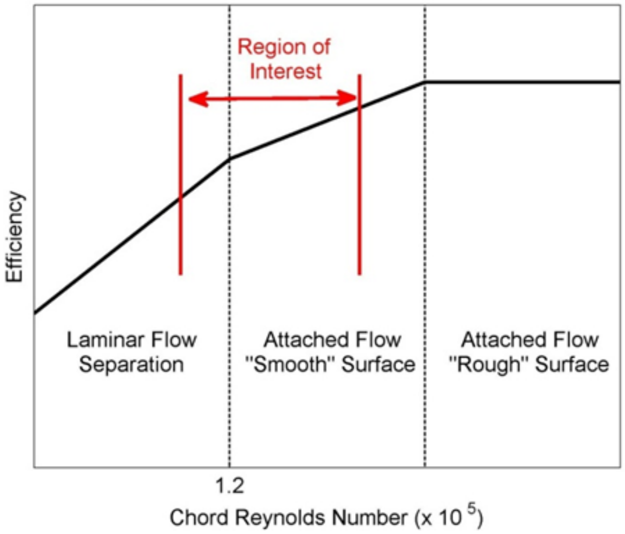

Figure 3-3: Reynolds number regimes [26].

At Reynolds numbers greater than 10^6, the flow is hydrodynamically rough along the blades, making efficiency independent of Reynolds number. As the Reynolds number decreases through the hydrodynamically smooth flow regime, efficiency drops. Here, the boundary layers grow with decreasing Reynolds number, increasing stagnation pressure loss. At lower values, approximately $\mathrm{Re} = 1.2 \times 10^5$ for the machine shown here, there is a laminar separation, causing a sharp decline in compressor efficiency [26].

Our region of interest falls close to the laminar flow separation boundary. Although the smallest rotor Reynolds number is estimated to be 160,000, there is uncertainty in the laminar flow separation boundary found by Schaffler. Moreover, smooth blades will be assumed for this study, keeping the flow out of the 'rough' surface regime. Figure 3-3 illustrates our region of interest.

Loss coefficient,

$$\omega = \frac{P_{01} - P_{02}}{P_{01} - P_1} \tag{3.1}$$

is related to entropy generation,

$$\Delta s = -R \ln\left(1 - \omega\left(1 - \frac{P_1}{P_{01}}\right)\right) \tag{3.2}$$

and thus adiabatic efficiency as shown by Denton [5].

$$\eta_{adiabatic} = 1 - \frac{T_2 \Delta s}{\Delta h_0} \tag{3.3}$$

Figure 3-4 gives the increase in loss coefficient with decreasing Reynolds number for the 2D geometry of E^3 rotor at mid-span. The values in Figure 3-4 were found using MISES, a 2D cascade code, for the E^3 rotor mid-span geometry. The computational results show a similar trend to Robert's experimental results, which provide support for our results.

It has been found that as the turbulence level increases, the sensitivity to Reynolds number decreases. The large drop-off found by Roberts is thus expected to be mitigated due to higher turbulence levels in an operating HPC. For the Reynolds number investigation in this thesis, an HPC turbulence level of 5% was selected as suggested by Cumpsty for an HPC [4].

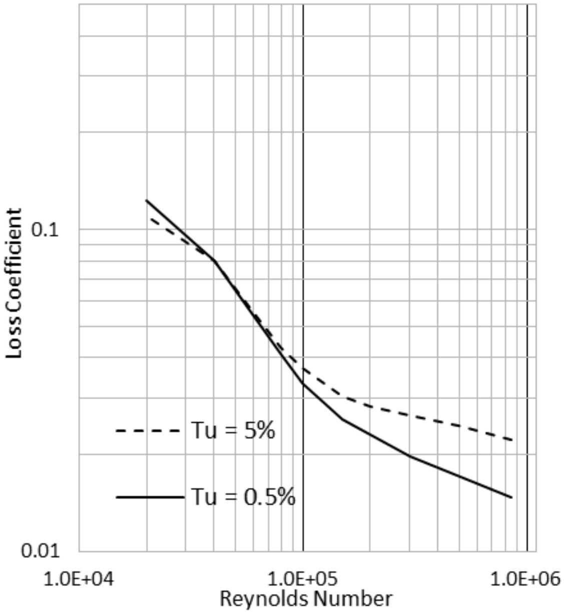

Figure 3-4: MISES computations of loss coefficient versus Re for E^3 rotor blade at different turbulence levels.

Blade flow turning is directly related to enthalpy rise though the Euler turbine equation. A modified version of this equation is presented in Equation 3.4.

$$\Delta h_0 = UV_x \left(\tan \alpha_1^{rel} - \tan \alpha_2^{rel}\right) \tag{3.4}$$

Figure 3-5 shows the deflection angle, defined as the change in relative flow angle from rotor inlet to outlet, at different Reynolds numbers to illustrate the effect on work output. For a relative incidence angle of 60 degrees there is a decrease in turning from 15.5 degrees to 14 degrees leading to a 6.9% decrease in enthalpy rise.

Using the loss and turning angle for the E3 rotor and stator, we can estimate the stage efficiency, and calculations for adiabatic efficiency are presented in Appendix B. Figure 3-6 shows the effect of Reynolds number on efficiency for a baseline E^3 stage. For the lowest Reynolds number of interest in this thesis (Re = 160,000), there is approximately a 2.25% drop in efficiency compared to operation at Re = 1.1×10^6. The baseline of Re = 1.1×10^6 was selected as the highest Reynolds number found in the assumed 6.0 lbm/s compressor.

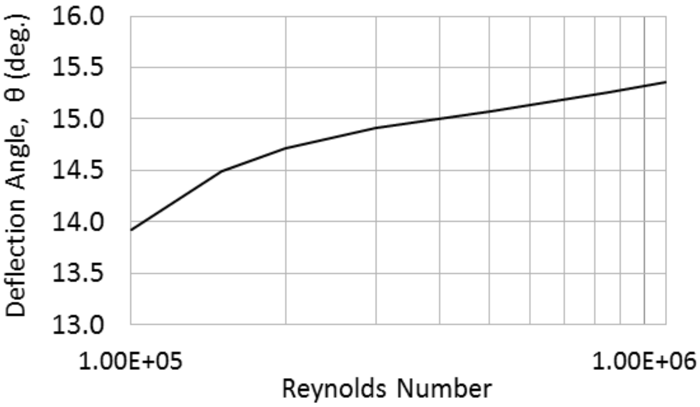

Figure 3-5: MISES calculations of deflection angle as a function of Reynolds number, E^3 blading, 2D flow, M=0.7, Tu=5%.

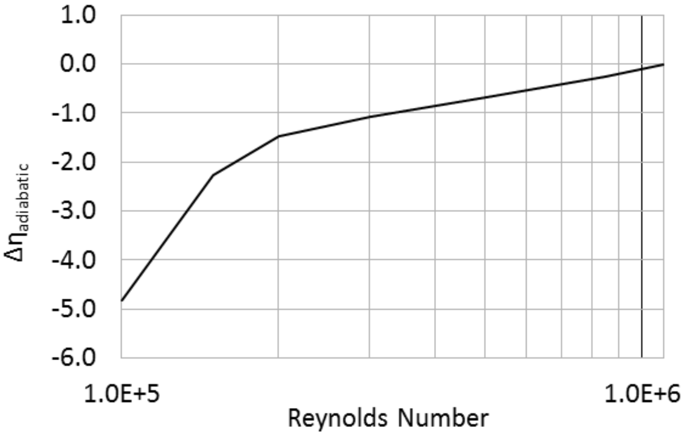

Figure 3-6: Decrease in adiabatic efficiency versus Reynolds number for a baseline stage. MISES calculations are for 2D flow at M=0.7, Tu=5%, ϕ=0.45. E^3 stage, baseline Re $= 1.1 \times 10^6$.

3.4 Optimization Procedure

The E^3 blades were designed to operate at a Reynolds number of 300,000 and the preceding results have thus been for blades not designed for a Reynolds number of 160,000. Airfoils have been optimized to operate at these low Reynolds numbers (for example the work of Drela [6]) and this can be also be done for compressor blades. For example, Honda was successful in optimizing a low pressure turbine guide vane by reducing the loss coefficient, ω, by 30% [28].

The potential benefits of airfoil optimization were assessed using the program MILOP for both the rotor and stator in conjunction with MISES to optimize cascade blades [8]. The program works by taking a starting geometry and defining the surfaces as Chebyshev polynomials. A Newton solver is employed to optimize geometry.

Because the focus of this research was to find the potential for aerodynamic improvement, structural constraints were ignored. However, two constraints were used, constant turning and constant solidity. Turning was held constant to keep the work the same in the optimized design as in the baseline E^3 design. (Reducing turning may increase individual stage efficiency, but it is difficult to objectively evaluate the performance drawbacks of additional stages.) Solidity was held constant to keep blade loading constant. The Reynolds number at the optimization point was rounded to 150,000.

The degrees of freedom for the optimizer were the stagger angle and the coefficients of the Chebyshev polynomials. Chebyshev polynomials were used to define the top and bottom surfaces of the airfoil and are useful because they give high resolution at the endpoints (compared to sine functions). Since aerodynamic performance has strong dependence on geometric features in the leading and trailing edge regions, the increased resolution allows for better designs. In the final optimization, a total of twenty Chebyshev polynomials were used to define the upper and lower surfaces (ten each).

The figure of merit was minimization of pressure loss, ω, over flow coefficients from 0.41 to 0.49. Efficiency is a function of both the loss and turning of the blade, but with turning held constant, increased efficiency corresponds to decreased loss. The design point is ϕ=0.45 and the optimization was performed over five equally spaced points points ranging from ϕ=0.41 to ϕ=0.49, which spans 10% to either side of the design flow coefficient of 0.45. All points were weighted the same. The optimization description is depicted in Figure 3-7.

Constraints

- Turning same as E^3 (same work)
- Solidity same as E^3 (same loading)

Perturbation Modes

- Blade surfaces defined by Chebyshev polynomials
- Blade angle

Figure of Merit

- Minimize loss coefficient, ω, for flow coefficients of 0.41-0.49.

Figure 3-7: Optimization routine set-up.

3.4.1 Optimized Rotor Blade

The optimized rotor blade, using the minimum ω figure of merit, is given along with the original E^3 blade in Figure 3-8. The aerodynamic and geometric properties of the two blades are summarized in Table 3.3.

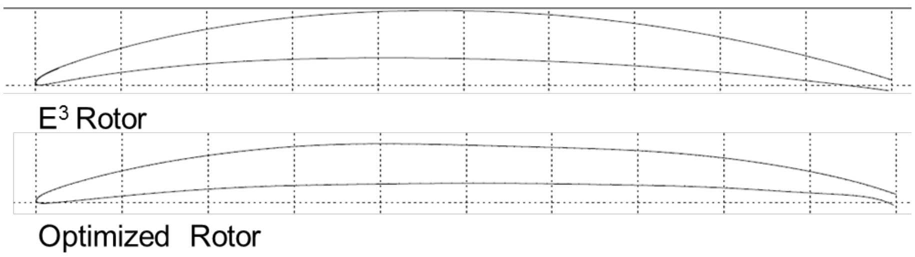

Figure 3-8: Geometries of the E^3 rotor and optimized rotor.

	Baseline	Optimized	Change
$\Sigma\omega$	0.0601	0.0393	-34.6%
Σc_y	0.4218	0.4270	1.2%
Thick/Chord	0.0622	0.0522	-16.1%
Area	0.0462	0.0400	-13.4%
Strain	2154	3158	46.6%

Table 3.3: Aerodynamic and geometric properties of baseline E^3 and optimized rotor blades.

There are several geometric changes in the optimized rotor blade compared to the E^3 blade. Most noticeably, the optimized blade is thinner. The maximum thickness/chord value changes from 6.2% to 5.2%. The total area decreases by 13%.

An interesting feature of the optimized blade is the divergent trailing edge (DTE) output from the optimizer. The divergent trailing edge, depicted in Figure 3-9, is a relatively recent discovery found only after the development of computational design tools [17]. The divergent trailing edge has three primary characteristics. First, the trailing edge has a finite thickness. Second, the lower surface has increasing curvature toward the rear of the blade. Third, the angles of the upper and lower surfaces diverge.

The DTE has a number of advantages. If the trailing edge thickness is kept to less than 1% of the chord length, the loss incurred is no greater than a zero thickness trailing edge. Next, the increased surface curvature near the rear of the blade leads to additional turning. Third, the DTE allows the Cp distributions on the upper and lower surfaces to be decoupled. This is particularly useful for the optimizer as it can better tailor each of the Cp distributions to minimize loss and retain turning [17].

The optimized rotor blade reduces loss over the range of flow coefficients from 0.41 to 0.49. Figure 3-10 illustrates the point by displaying loss for both the baseline E^3 and optimized blades. The x-axis in Figure 3-10 is flow coefficient and the y-axis is loss coefficient. The optimized blade reduces loss by an average of 35% over all flow coefficients investigated and by 27% at design.

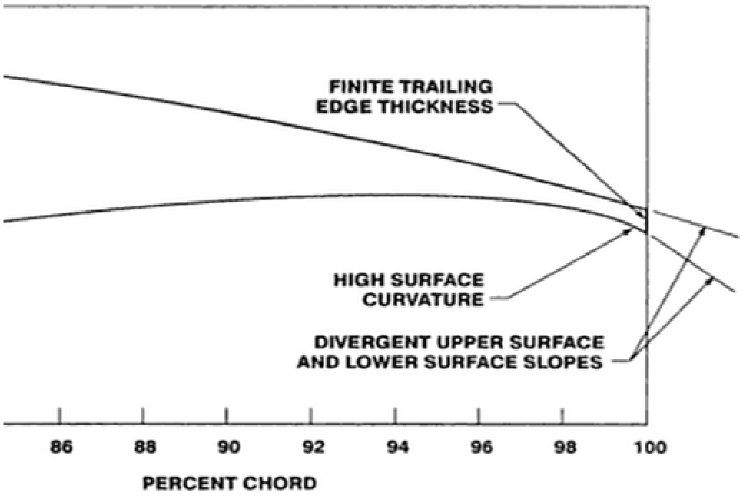

Figure 3-9: Illustration of a Divergent Trailing Edge (DTE), Reproduced from *Applied Computational Aerodynamics*, P.A. Henne [17].

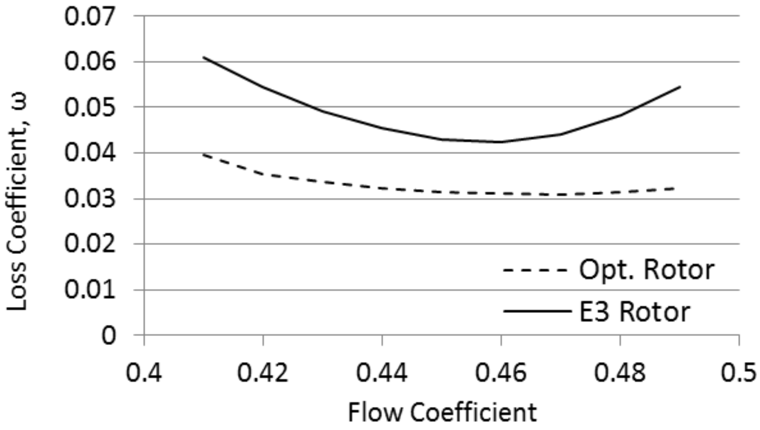

Figure 3-10: Loss coefficient versus incidence angle for E^3 and optimized rotor blades.

3.4.2 Optimized Stator Vane

The stator vane was also optimized for low Reynolds number conditions. The stator vane operates at a Reynolds number lower than the rotor blade because the relative velocities are smaller. For a rotor Reynolds number of 150,000, the stator has a Reynolds number of 108,000. Figure 3-11 shows stator Reynolds number through a shaft limited HPC. The x-axis is stage and the y-axis is stator Reynolds number.

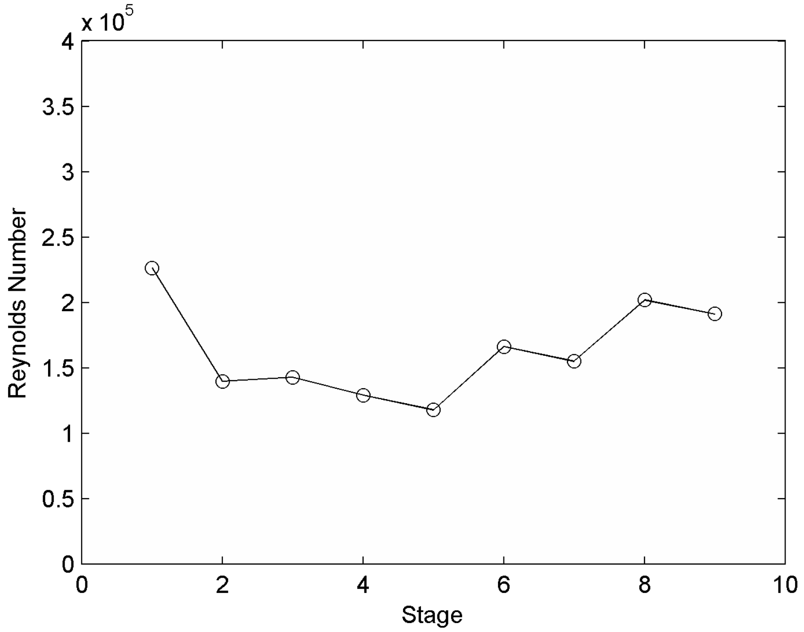

Figure 3-11: Stator Reynolds numbers at different stages in the D8.6 axial compressor for a shaft limited configuration at a core size of 1.5 lbm/s.

Figure 3-12 shows the geometry of the baseline and the optimized stators and it can be seen that the optimized stator has a thinner profile. Table 3.4 summarizes the properties of the two vanes.

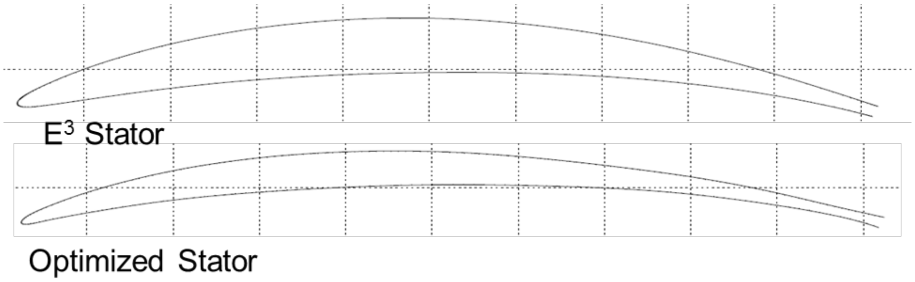

Figure 3-12: E^3 stator geometry and optimized stator geometry.

	Baseline	Optimized	Change
$\Sigma\omega$	0.0422	0.0314	-25.5%
Σc_y	0.4978	0.5008	0.6%
Stagger Angle (deg.)	31.4	31.8	0.4
Thickness/Chord	0.0752	0.0485	-35.5%
Area	0.0535	0.0332	-38.0%
Strain	1429	3290	130.2%

Table 3.4: Aerodynamic and geometric properties of baseline E^3 and optimized stators.

As with the rotor, a reduction in stagnation pressure loss is observed, 26% compared to 35% for the rotor blade. To achieve this improvement, the optimized stator underwent a number of geometric changes. The thickness/chord ratio decreased from 7.5% to 4.9% and the area was reduced by 38%. This led to a much thinner design. (Again, structural assessment was not carried out). The improvement in loss mitigation is not as much as the rotor blade despite the larger changes in geometry, implying there is more to be gained through optimization of the rotor blade for low Reynolds number flow than optimization of the stator vane.

The optimized stator reduces loss over a broad range, but exhibits stalling behavior at the lowest flow coefficient of interest. Figure 3-13 illustrates the loss coefficient of the optimized stator at different flow coefficients. In Figure 3-13, the x-axis is flow coefficient and the y-axis is loss coefficient. Taking a weighted average over the entire operating range, the optimized stator reduces loss by 26% and by 18% at the on design point.

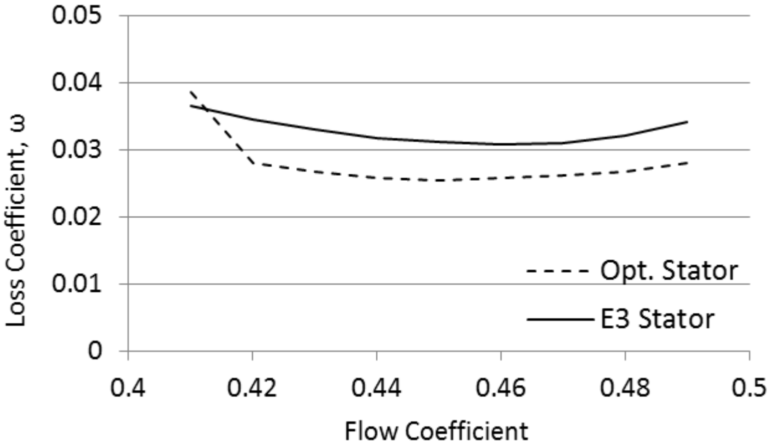

Figure 3-13: Loss coefficients for the E^3 and optimized stators as a function of flow coefficient.

3.5 Efficiency Improvement of the Optimized Stage

Stage adiabatic efficiencies for both the baseline E^3 and optimized stages are shown in Figure 3-14 . Efficiency benefits are seen at all Reynolds numbers of interest for the optimized blading. Even at $\text{Re} = 1.1 \times 10^6$, a 1.1% improvement in efficiency is obtained, likely due to the thinner profiles of the optimized blades. Larger efficiency improvements are seen at lower Reynolds numbers. At the optimization point of Re=150,000, efficiency is increased by 1.6% and at an even lower Reynolds number of 100,000, efficiency is improved by 3.0%. This shows that blade optimization is more useful at lower Reynolds numbers.

Efficiency calculations were also run at off-design conditions for Reynolds numbers of 150,000, 300,000, and 1.1×10^6 and plots of efficiency versus flow coefficient for the E^3 and optimized blades are given in Figures 3-16 and 3-17. In both figures, the x-axis is flow coefficient and the y-axis is adiabatic efficiency. The curves for the optimized stage are flatter, indicating less sensitivity to off-design operation.

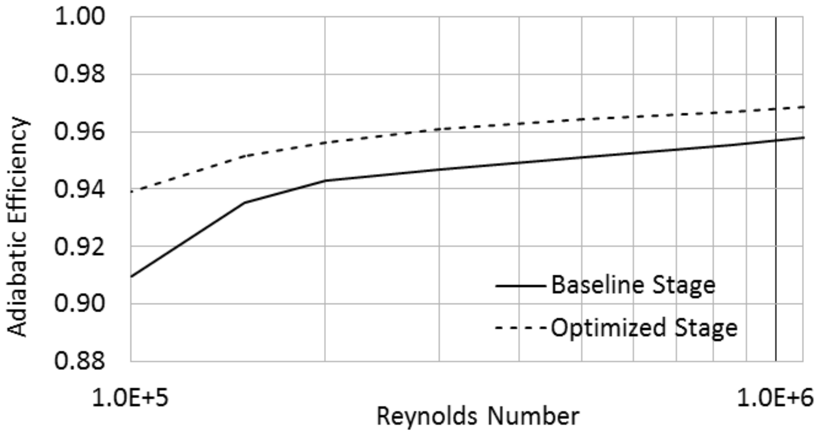

Figure 3-14: Adiabatic efficiency versus Reynolds number for baseline E^3 and optimized stages.

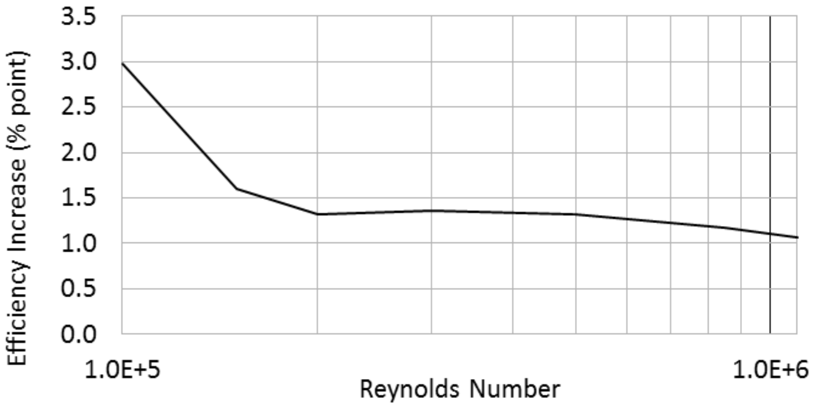

Figure 3-15: Adiabatic efficiency increase for the optimized stage over the baseline E^3 stage.

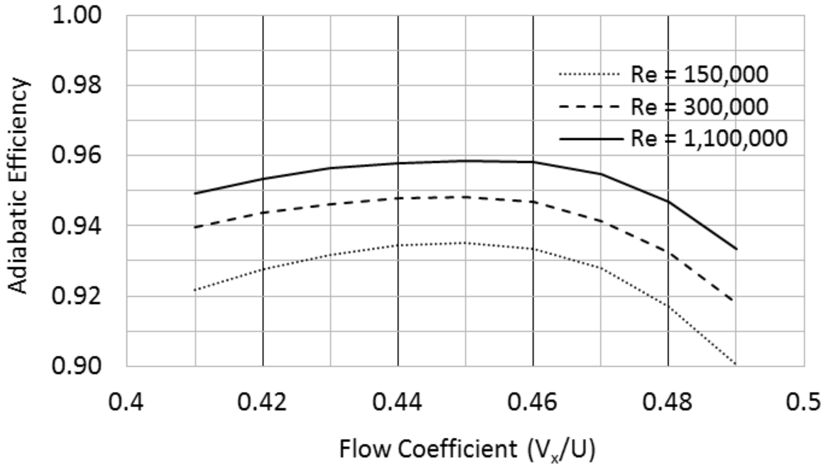

Figure 3-16: Off-design efficiency for baseline E^3 stage. Efficiency versus flow coefficient at different Reynolds numbers.

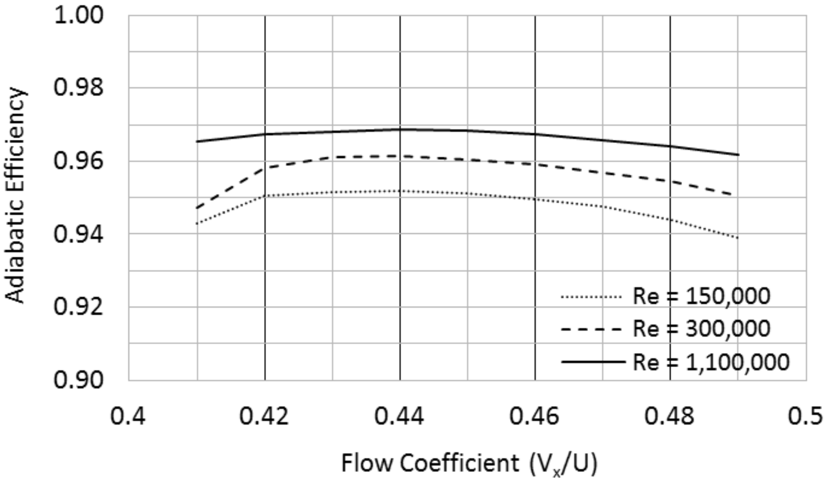

Figure 3-17: Off-design efficiency for optimized stage. Efficiency versus flow coefficient at different Reynolds numbers.

3.6 Reynolds Number Efficiency Penalty at Different Core Sizes

In Section 3.1, three distinct compressor configurations were introduced. The bulk of this chapter has focused on the shaft limited design, which has a minimum rotor Reynolds number of 160,000. However, the findings are applicable to Reynolds numbers of 100,000 to 1.1×10^6 and can be applied to compressors of different core sizes. In this section, we quantify the Reynolds number efficiency penalty for core sizes of 1.0 lbm/s to 6.0 lbm/s.

Figure 3-18 shows maximum efficiency penalty as a function of core size. Efficiency penalty is the efficiency reduction compared to a baseline value. The x-axis is core size and the y-axis is maximum efficiency penalty related to a pure scale 6.0 lbm/s HPC. From Figure 3-18, it is seen that compressor configuration has a strong impact on the Reynolds number efficiency penalty. For a pure scale machine, there is a 0.6% reduction in stage efficiency for a compressor size of 1.5 lbm/s. This penalty is magnified if the machine is shaft limited, where efficiency penalty grows to 1.2%. A shaft removed machine is only marginally affected by Reynolds number, with an efficiency penalty of 0.2% at a compressor size of 1.5 lbm/s.

Similar calculations were conducted for the optimized blading and Figure 3-19 illustrates efficiency penalty versus core size for the optimized stage. Comparing Figures 3-18 and 3-19, there is an small efficiency benefit of the optimized stage, ranging from 0.01%-0.2%. Table 3.5 summarizes these results. Even though Section 3.5 showed that an optimized stage can increase efficiency by 1.6%, since the baseline 6.0 lbm/s compressor is assumed to incorporate the optimized blades (which tend to increase efficiency at all Reynolds numbers), there is a much smaller benefit to the optimization.

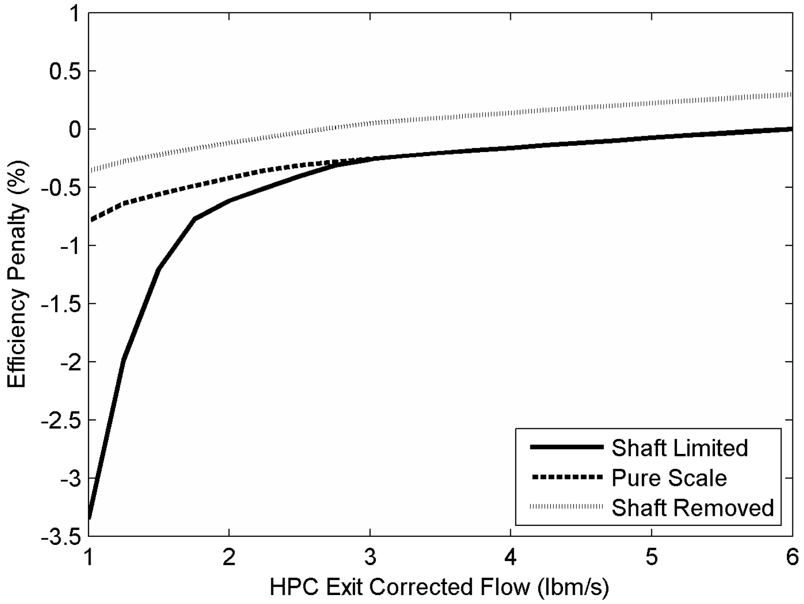

Figure 3-18: Reynolds number stage efficiency penalty for baseline E^3 blading. Baseline core, 6 lbm/s.

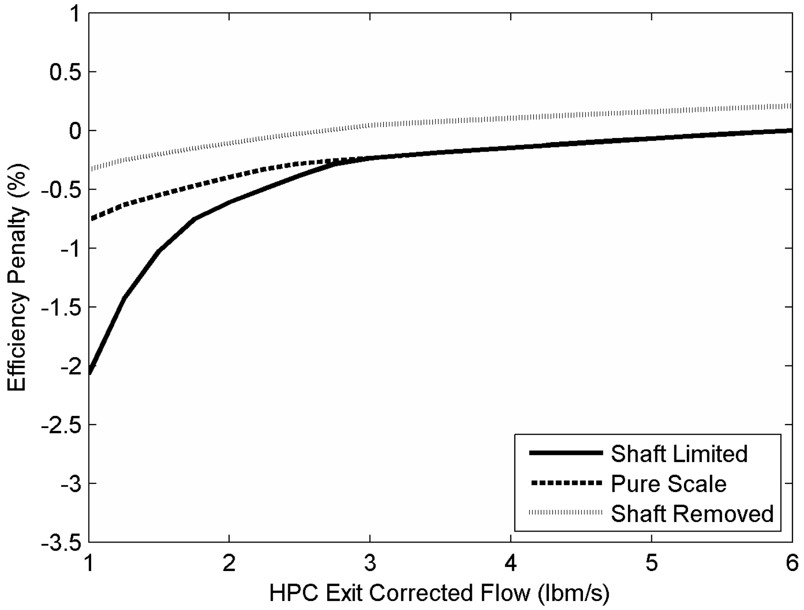

Figure 3-19: Reynolds number stage efficiency penalty for optimized blading. Baseline core, 6 lbm/s.

	Compressor Configuration		
	Shaft Limited	Pure Scale	Shaft Removed
Baseline Blading	-1.20%	-0.56%	-0.22%
Optimized Blading	-1.02%	-0.55%	-0.20%
Optimization Benefit	0.18%	0.01%	0.02%

Table 3.5: Maximum Reynolds number stage efficiency penalty for a 1.5 lbm/s core compared to a 6.0 lbm/s core.

3.7 Summary of Low Reynolds Number Effects on Compressor Efficiency

The results of the two-dimensional calculations can be summarized as follows.

1. Rotor Reynolds number is dependent on compressor configuration and can vary by roughly a factor of two (160,000 vs. 309,000) for the same corrected flow.
2. The lowest rotor Reynolds number for a 1.5 lbm/s shaft limited machine was found to be 160,000. The lowest stator value was 108,000.
3. A stage efficiency drop of 2.3% was found for operation at a $Re = 150,000$ compared to $Re = 1.1 \times 10^6$ (2D flow, M = 0.7).
4. Blade optimization can improve stage efficiency by 1.6% at Re = 150,000.
5. Optimization of the rotor blade is more beneficial than optimization of the stator vane.

For a core size reduction from 6.0 lbm/s to 1.5 lbm/s, the results show:

1. The stage efficiency penalty is up to 1.2% in a shaft limited machine, but only up to 0.2% in a shaft removed configuration.
2. Optimized blading offers a 0.2% increase in efficiency at compressor size of 1.5 lbm/s for a shaft removed configuration. The increase is not the full 1.6%

cited in Section 3.5 because the baseline 6.0 lbm/s core is assumed to have the optimized blades (which tend to increase efficiency at all Reynolds numbers).

3. Optimized blading offers a 0.01%-0.02% increase in efficiency for the pure scale and shaft removed configurations. This occurs because the pure scale and shaft removed configurations have Reynolds numbers no smaller than 225,000 at a core size of 1.5 lbm/s. The sensitivity of efficiency to Reynolds number is small at 225,000 compared to 160,000 for both the baseline and optimized stages (see Figure 3-14).

4. The benefits of optimized blading increase as compressor size decreases below 1.5 lbm/s.

Chapter 4

Estimates of Tip Clearance Losses in Small Core Compressors

4.1 Introduction

Compressors have a tip clearance, or tip gap, between the end of the rotor blade and the casing shroud defined non-dimensionally as ε/S. Flow leaks through this gap and mixes with the mainstream flow, producing a loss. For compressor stages with a 1% clearance-to-span ratio, over 20% of the total loss can be attributed to the tip clearance flow [15]. An expression for the entropy increase associated with tip clearance flow is given in Equation 4.1 [5].

$$T\Delta s_{tot} = \frac{C_d \varepsilon C}{V_2 S\, p\, \cos\alpha_2} \int_0^1 V_s^2 (1 - \frac{V_p}{V_s}) \sqrt{(V_s^2 - V_p^2)} \frac{dz}{C} \tag{4.1}$$

The entropy rise is proportional to gap size because the leakage flow is proportional to gap size.

4.1.1 Factors that Set Tip Clearance and Tip Clearance Scaling

The physical clearances in high pressure compressors are measured in mils, with a representative value for a 6 lbm/s core being 12 mils[1] and it is not obvious how the clearance will scale as the physical size of a compressor decreases. This section discusses factors that affect the tip clearance.

Variations in blade and case size are primary factors. The tip clearance of concern to us is the clearance during cruise. The clearance is set by the difference in rotor and case size from the "pinch point" (the operating condition where there is no clearance between the rotor and case) and the cruise condition. Thermal loading (heating) causes the blades and case to increase in size as they increase in temperature. Equation 4.2, gives the thermal growth of the blades, with GR being the rotor blade growth, r the radius, and α the coefficient of thermal expansion.

$$GR_{thermal} = r\alpha\triangle T \tag{4.2}$$

The blades also grow because of centrifugal forces,

$$\Delta GR_{centrifugal} = r^2\Omega^2 \tag{4.3}$$

For specified axial velocity and velocity triangles, the value $r\Omega$ remains constant, so centrifugal growth does not vary with core size if these are maintained.

There are many additional effects in a compressor involved in determining tip clearance. These values may or may not scale with core size,

1. Engine vibrations (e.g. whirl).
2. Aircraft maneuvering and thrust loads (e.g. backbone bending).
3. Case out of roundness.
4. Manufacturing tolerances.

---

[1] From discussion with Pratt and Whitney [1].

5. Rub systems.

4.1.2 Assumed Clearances

The above only scratches the surface, but the point is that it is difficult to accurately predict how tip clearances will change with compressor size because of the many influences. We will therefore use two assumptions to bound the problem.

The first of these is to assume constant physical clearance (i.e. clearances not scalable). If we take our representative tip clearance of 0.012 inches for a 6 lbm/s core, the constant physical clearance approximation would keep clearance at 0.012 inches, regardless of compressor size.

A second and quite different assumption is that the clearance scales with radius. In other words, as radius decreases, physical tip clearance also decreases, keeping the value ε/r_{mean} constant. This assumption leads to efficiencies that are higher than the first assumption.

Figure 4-1 shows non-dimensional tip clearance as a function of stage for the shaft limited configuration at two core sizes. The x-axis is stage and the y-axis is non-dimensional tip clearance. The solid lines represent the constant physical clearance assumption and the dashed lines represent the scalable assumption. Lines marked with a circle are for a 1.5 lbm/s core and lines marked with a diamond are for a 3.0 lbm/s core.

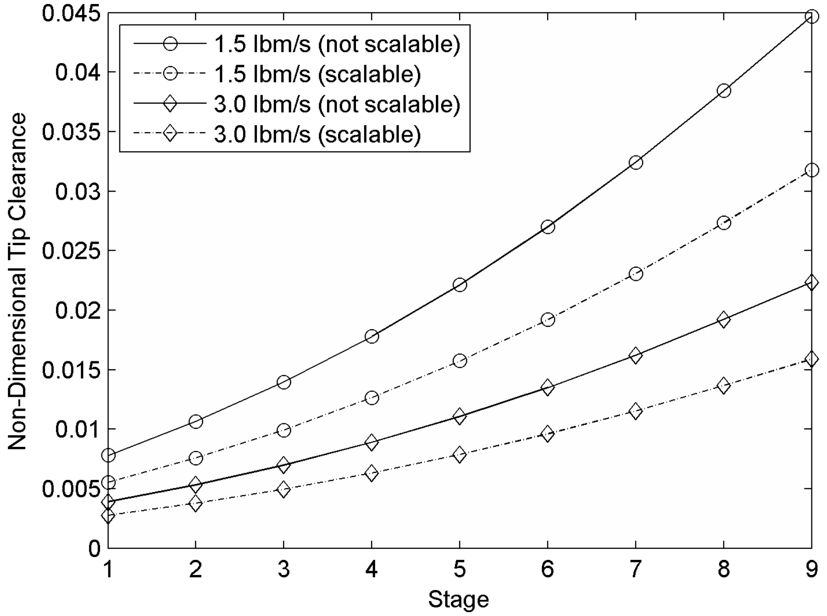

Figure 4-1: Tip clearance, ε/S, versus stage and core size for a shaft limited configuration. Not scalable (constant tip clearance) and scalable clearance shown as solid and dashed lines respectively.

The differences between the two tip clearance assumptions at 1.5 lbm/s are tabulated in Table 4.1 for the three configurations defined in Chapter 3. Table 4.1 shows how minimum blade height and maximum tip clearance are affected by compressor configuration and assumptions about tip clearance scaling. The difference between the two scaling assumptions is roughly1.4% clearance for the three configurations.

	Configuration		
	Shaft Limited	Pure Scale	Shaft Removed
Min. Blade Height	0.26 in	0.33 in	0.50 in
Max. ε/S (clearances not scalable)	4.5%	3.1%	2.1%
Max. ε/S (clearances scalable)	3.2%	1.6%	0.7%

Table 4.1: Maximum tip clearance for three compressor configurations at 1.5 lbm/s.

Tip Clearances in a Pure Scale Compressor Configuration

For the pure scale compressor configuration, the non-dimensional tip clearance will remain constant at all core sizes using the scalable clearance assumption, because blade span in a pure scale machine also scales with radius. The blade span is given by

$$S = r_{tip}(1 - \frac{r_{hub}}{r_{tip}}) \tag{4.4}$$

or,

$$S \propto r_{tip}$$

Tip gap, ε, is also proportional to radius so scalable clearance means the non-dimensional clearance is not dependent on core size.

Tip Clearances in a Shaft Removed Configuration

The shaft removed configuration has substantially lower non-dimensional tip clearance values than the pure scale configuration. Even when the clearances not scalable assumption is employed, the non-dimensional clearance is reduced when there is no LP shaft constraint. This occurs because blade heights increase to keep flow area constant when radius is decreased as shown below. The flow area is

$$A = 2\pi r_{mean} S \tag{4.5}$$

blade span is

$$S = \frac{A}{2\pi r_{mean}} \tag{4.6}$$

and the clearance-to-span ratio is thus

$$\varepsilon/S = \frac{\varepsilon 2\pi r_{mean}}{A} \tag{4.7}$$

Equation 4.7 shows for a shaft removed configuration, where r_{mean} is reduced from the pure scale value, clearance-to-span ratio decreases compared to the pure scale value at the same flow area. Even though physical gap remains constant, r_{mean} decreases, which means that the gap leakage area decreases.

The shaft removed configuration has even smaller tip clearance values using the scalable tip clearance assumption because the reduction in mean radius decreases the physical tip clearance. This is shown in the last column of Table 4.1; the maximum tip clearance for the shaft removed configuration is 0.7% gap-to-span ratio.

4.1.3 The Embedded Stage

Many authors have commented on the complexity of the flow through a multistage axial compressor which is, in the words of Carter, “academically depressing.”[2] A useful observation, however, is that after the first 2-4 stages, the flow velocity profile into each stage becomes close to the velocity profile out of the stage. This phenomenon has been referred to as the “ultimate steady flow” by Howell [19] and “equilibrium profile” by Mellor and Strong [22]. This thesis will use the terminology ultimate steady flow and a stage that has an ultimate steady flow will be referred to as an “embedded stage.”

Smith examined factors such as pressure rise, tip clearance, and aspect ratio, that influence the features of the ultimate steady flow and found that tip clearance variations were important in determining the inlet velocity profile of the ultimate steady flow [27]. We will use the work of Smith to estimate inlet velocity profiles for different tip clearances with the goal of providing a simple approximation to an embedded stage. For each tip clearance value investigated, an approximate ultimate steady flow will be used as the inlet condition.

---

[2] As quoted in Smith [27].

4.1.4 Approach

To accurately determine the efficiency penalty associated with tip clearances in an embedded stage environment, multistage computations or experimentations are needed. In the interest of time and to keep within the scope of the thesis (determining estimates of small core compressor efficiency), the embedded stage approximations suggested by Smith, plus isolated rotor calculations, were used to get insight into trends in the efficiency penalty associated with tip clearances in an embedded stage.

The data show that as tip clearance changes, so does the velocity profile into an embedded stage. Using Smith's analysis [27], a rotor inlet flow profile will be constructed that estimates an ultimate steady flow for tip clearances from 1%-6%. This estimated profile is then used as the input to an isolated rotor to estimate clearance losses for gap-to-span ratios up to 6%. The results provide a way to assess the impact of tip clearance for the three compressor configurations introduced in Chapter 3.

4.2 CFD Computations

4.2.1 Computation Setup

Calculations of flow through the rotor were carried out using the FINE/Turbo code. The compressor geometry used was that of the NASA Large Low-Speed Axial-Flow Compressor (LSAC). The LSAC is modeled after the GE Low-Speed Research Compressor and is designed to provide accurate low speed simulation of a high speed multistage compressor. Baseline parameters for the LSAC are provided in Table C.1 [29].

The blading used is based on the Rotor B / Stator B geometry created by General Electric [29]. Modifications were made to the NASA LSAC blades to account for the difference in hub-to-tip ratio between the General Electric and NASA versions and a description of the blading is given in Wellborn [29].

For the computations, the Reynolds-Averaged Navier Stokes (RANS) equations were solved using the k-omega Shear Stress Transport (SST) model. This two equation model incorporates aspects of k-omega and k-epsilon modeling. In the inner parts of the boundary layer, k-omega is used. In the free stream, k-epsilon is used. SST was chosen as it is robust at low Reynolds numbers [23].

4.2.2 Rotor Row Parameters

The geometry and mesh for the isolated rotor row are seen in Figure 4-2. Details of the E^3 blading and the mesh are listed in Tables 4.2 and 4.3 respectively. A relative Reynolds number of 2.15×10^5 was used based on the rotor Reynolds number at the last stage in a 1.5 lbm/s shaft limited HPC.

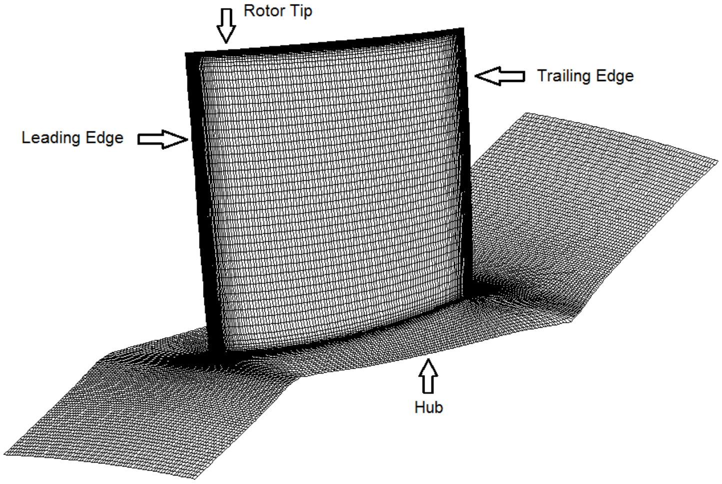

Figure 4-2: Mesh on the hub and blade surface.

Work Coefficient	0.550
Flow Coefficient	0.400
Mid-span Relative Inlet Angle	68.9 deg.
Mid-span Relative Exit Angle	37.1 deg.
Solidity	1.15
Aspect Ratio	1.20
Relative Reynolds Number	2.15x10^5

Table 4.2: Rotor parameters.

Cell Count	2.97 x 10^6
Average Near-Wall y+	0.4
Cells Across Tip Gap	41
Domain Inlet Location (chords upstream of LE)	1.46
Domain Exit Location (chords downstream of TE)	2.01

Table 4.3: Mesh details.

4.2.3 Embedded Stage Velocity Profiles

The third stage of the NASA LSAC compressor becomes an embedded stage when run near peak efficiency as can be seen from the axial and tangential velocity profiles into and out of the third stage in Figures 4-3 and 4-4 [29]. The profiles are for rotor tip clearances of 1.4%. Large differences in the flow were observed from rotor to stator, but not across the stage, indicating that the ultimate steady flow concept can be applied.

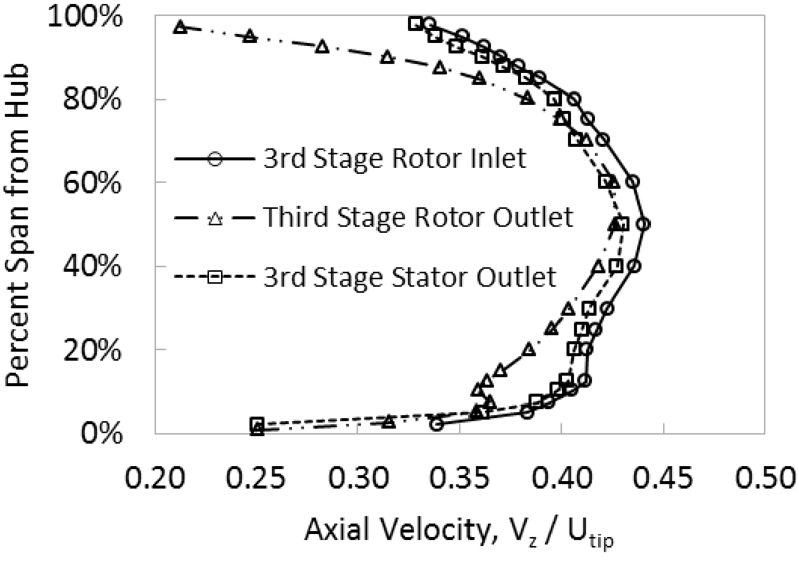

Figure 4-3: Measured third stage axial velocity profiles with 1.4% tip clearance [29].

A primary characteristic of the boundary layers in Figure 4-3 is the displacement thickness, $\delta *$, defined as the distance by which the boundary would have to be moved

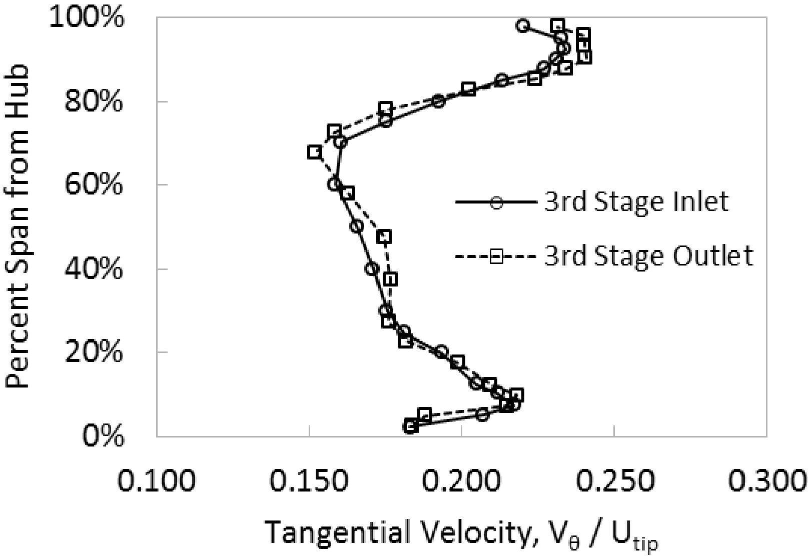

Figure 4-4: Measured third stage tangential velocity profiles for 1.4% tip clearance [29].

to give the same mass flow rate if no boundary layer existed. The formula for displacement thickness is given in Equation 4.8 where V is velocity and r is radius. The tilde indicates free stream values.

$$\delta_t * = \frac{1}{r_t \tilde{V}_{zt}} \int_{r_t-\delta_t}^{r_t} \left(\tilde{V}_z - V_z\right) r\, dr \tag{4.8}$$

Table 4.4 lists the displacement thickness at the rotor inlet, rotor outlet, and stator outlet in terms of span. The displacement thickness increases through the rotor row and decreases through the stator.

	Rotor Inlet	Rotor Outlet	Stator Outlet
Displacement Thickness, $\delta * /S$	0.0295	0.0492	0.0279

Table 4.4: Displacement thickness through the LSAC third stage. Tip clearances 1.4%.

4.2.3.1 Axial Velocity Profiles

In approximating an embedded stage environment, inlet velocity profiles were set based on Smith's analysis [27]. For the axial component of inlet velocity, Smith provides an estimate for the displacement thickness of an ultimate steady flow at different tip clearances as

$$\frac{\delta*}{g} = \frac{\delta*}{g}|_{\varepsilon/g=0} + \frac{\psi'}{\psi'_{max}} \cdot \frac{\varepsilon}{g} \tag{4.9}$$

where g is the blade stagger spacing and ψ' is the stage pressure rise coefficient.

The term representing the ultimate steady flow displacement thickness at 0% clearance can be found using the measured results ($\delta*$, $\psi'$and ψ'_{max}) at 1.4% clearance and Equation 4.9 [29]. To determine the pressure rise coefficient at clearance values 1%-6%, the results of CFD calculations (different tip clearances with the inlet profile that of Figure 4-3) were used. Maximum pressure rise coefficients, ψ'_{max}, were estimated using the experimental trend found by Smith for different tip clearances [27]. Table 4.5 summarizes the parameters of the estimated ultimate steady flow for clearances 1%-6%.

Clearance, ε/S	ψ'	ψ'_{max}	$\frac{\delta*}{g}$	$\delta*/S$
1.0%	0.502	0.562	0.0389	0.0265
1.4%	0.495	0.555	0.0443	0.0302
2.0%	0.485	0.545	0.0517	0.0352
4.0%	0.444	0.510	0.0774	0.0526
6.0%	0.417	0.477	0.1029	0.0700

Table 4.5: Estimated embedded stage boundary layer displacement thickness for different clearances. $\frac{\delta*}{g_t}|_{\varepsilon/g_t=0} = 0.026$

The estimated axial velocity profiles are shown in Figure 4-6. These profiles have a displacement thickness as in Table 4.5. The profiles were generated by interpolating rotor *outlet* axial velocity profiles from the computations (different tip clearances with the inlet profile that of Figure 4-3) to give the rotor *inlet* displacement thickness, given in Table 4.5. The assumption made is that the shape of the outlet axial velocity profile from a rotor row is similar to that of the embedded stage inlet velocity profile. This cannot be correct, but it should reflect the overall trends. Figure 4-5 shows rotor exit axial velocity profiles from CFD calculations.

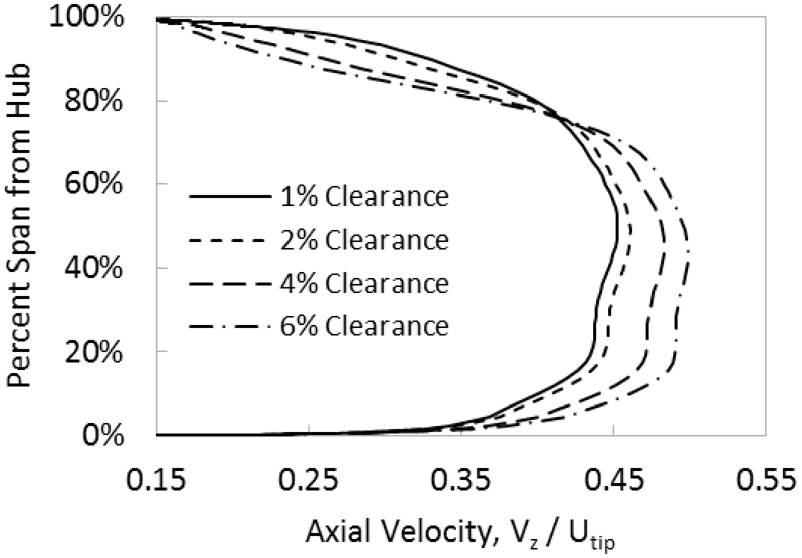

Figure 4-5: Rotor exit velocity profiles from CFD calculations using the inlet axial velocity of (Figure 4-3).

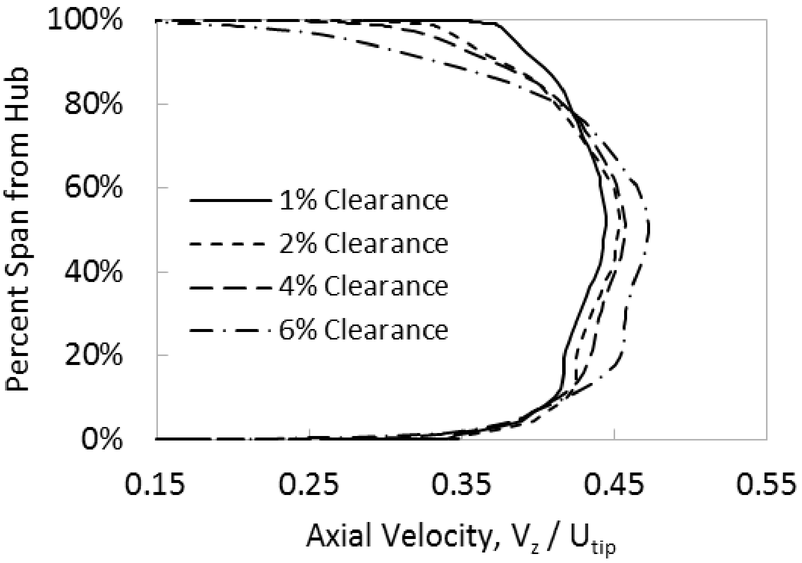

Figure 4-6: Embedded stage axial velocity profiles at the inlet.

4.2.3.2 Tangential Velocity Profiles

We also need to estimate the tangential velocity profile of the embedded stage. Smith and others have attempted to use the the tangential force thickness to describe this profile [27]. The tangential force thickness, denoted by υ, is related to the tangential force defect in the endwall boundary layer and is given by

$$\upsilon = \frac{1}{r_t \tilde{F}_{\theta t}} \int_{r_t - \delta_t}^{r_t} \left(\tilde{F}_\theta - F_\theta \right) r \, dr \tag{4.10}$$

where

$$F_\theta = 2\pi r_2 \rho V_{z2} \left(\frac{r_2 V_{\theta 2} - r_1 V_{\theta 1}}{r_{avg}} \right) \tag{4.11}$$

Shear stresses on the hub and casing walls are neglected in this formulation. Hunter and Cumpsty [20], and Smith [27], did not find a strong correlation between pressure rise, tip clearance, and tangential force thickness.

In the work here, we assume the rotor inlet flow angle does not depend on tip clearance. Some justification for this is provided in experiments by Howard and

Ivey who found that the flow angles in an ultimate steady flow are not affected by tip clearances from 1.2% to 3.0% [18]. We further assume the flow angles do not change for clearances up to 6.0%. The flow angles found by Wellborn and used in the embedded stage analysis are shown in Figure 4-7.

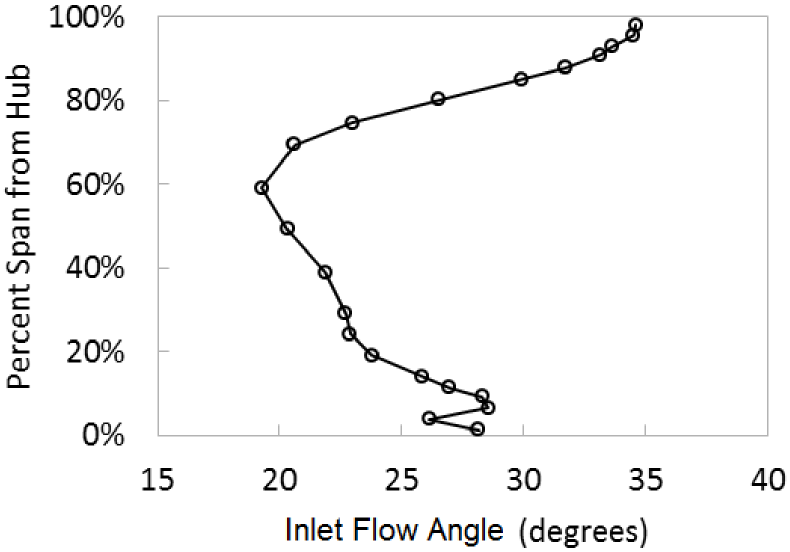

Figure 4-7: Rotor inlet flow angle used for embedded stage calculations [29].

4.2.4 Performance Calculation Methodology

For this study, polytropic efficiency is the performance metric of primary concern. The polytropic efficiency of a compression stage is defined as

$$\eta_p = \left(\frac{\gamma - 1}{\gamma}\right) \left[\ln\left(\frac{P_{t2}}{P_{t1}}\right) / \ln\left(\frac{T_{t2}}{T_{t1}}\right)\right] \tag{4.12}$$

The calculated polytropic efficiency is dependent on the locations chosen as rotor inlet and outlet planes. For this study, inlet and outlet conditions were determined 10% chord-length upstream and downstream of the rotor blade as indicated in Figure 4-8.

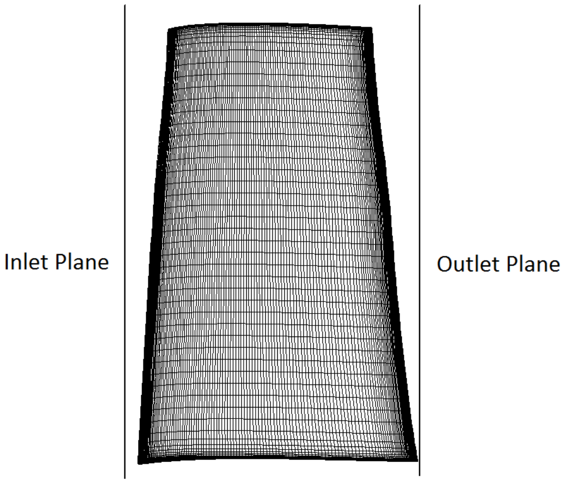

Figure 4-8: Locations of inlet and outlet measurement planes in the isolated rotor row computations.

Mass-average stagnation pressure (P_{t1}) and temperature (T_{t1}) upstream of the blade were used while a mixed-out value (based on a constant area mixed-out state) of P_{t2} and T_{t2} were used downstream of the blade. The constant area mixed-out calculation takes the flow at the outlet plane (see Figure 4-8) and mixes the flow using (two-dimensional) conservation of mass, momentum, and energy to a theoretical uniform state. A mixed-out value was used to account for the mixing losses that occur downstream of the rotor row. The three conservation equations solved for

- Conservation of Mass

$$\int_A \rho u_z dA = \rho_e u_{z_e} A = \dot{m} \tag{4.13}$$

- Conservation of Momentum (2-D approximation, axial and tangential directions only).

$$\int_A (p_i + \rho u_z^2) dA = \left(p_e + \rho_e u_{z_e}^2\right) A \tag{4.14}$$

$$\int_A (\rho u_\theta u_z) dA = \left(\rho u_{\theta_e} u_{z_e}\right) A \tag{4.15}$$

- Conservation of Energy for a perfect gas.

$$\frac{1}{\dot{m}}\left(\int_A(\rho u_z T_t)dA\right) = T_{t_e} \tag{4.16}$$

4.3 Results

4.3.1 Efficiency Reduction with Increased Tip Clearance

4.3.1.1 Baseline Axial Velocity Profile

Initial computations were run for clearances of 1%, 2%, 4%, and 6%, Reynolds numbers of 100,000 and 200,000, and the baseline inlet axial velocity profile (see Figure 4-3). The tip clearances chosen span the range of potential tip clearances summarized in Table 4.1. Reynolds numbers of 100,000 and 200,000 were chosen as they cover the range of Reynolds numbers expected for the shaft limited configuration (see Figure 3-2).

Polytropic efficiency as a function of tip clearance and Reynolds number is shown in Figure 4-9. The x-axis in Figure 4-9 is tip clearance and the y-axis is polytropic efficiency using mixed-out stagnation temperature and pressure as the outlet condition. The results of a linear regression analysis are tabulated in Table 4.6; a 1.1% decrease in polytropic efficiency was found for a 1% increase in tip clearance.

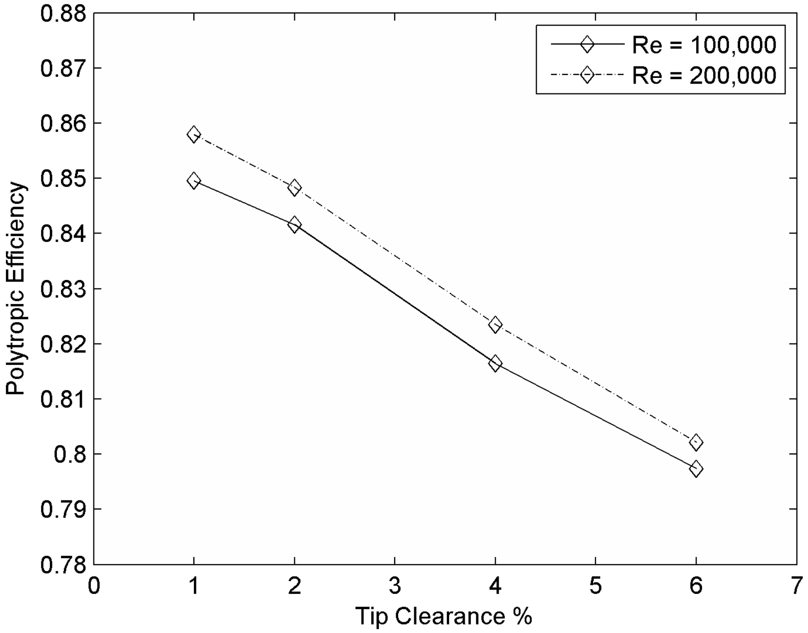

Figure 4-9: Polytropic efficiency for a single rotor row as a function of tip clearance for different Reynolds numbers. Inlet velocity profile of Figure 4-3, mixed-out stagnation temperature and pressure used as the outlet condition.

Re	100,000	200,000
Slope	-.0107	-.0113
y intercept	.861	.870
R^2	.997	.999

Table 4.6: Linear regression results for tip clearance data. Inlet velocity profile defined in Figure 4-3.

4.3.1.2 Embedded Stage Axial Velocity Profiles

Efficiency of the isolated rotor changes when the inlet conditions are set to the embedded stage velocity profiles given in Section 4.3.1.2 rather than the baseline profile of Figure 4-3. Figure 4-9 shows polytropic efficiency versus tip clearance for both the baseline and embedded stage inlet velocity profiles. The x-axis in Figure 4-9 is tip clearance and the y-axis is polytropic efficiency using mixed-out stagnation temperature and pressure as at the outlet. The efficiency for the embedded stage velocity profile has a greater falloff in efficiency with tip clearance than with the baseline profile. A linear regression analysis gives a 1.6% decrease in polytropic efficiency for every 1% increase in tip clearance for the rotor with an embedded stage inlet velocity profile. The regression is summarized in Table 4.7. The indication from these results is that incorporating an estimate for the change in inlet velocity profile associated with an embedded stage leads to a greater sensitivity of efficiency to tip clearance than if inlet displacement thickness was held constant.

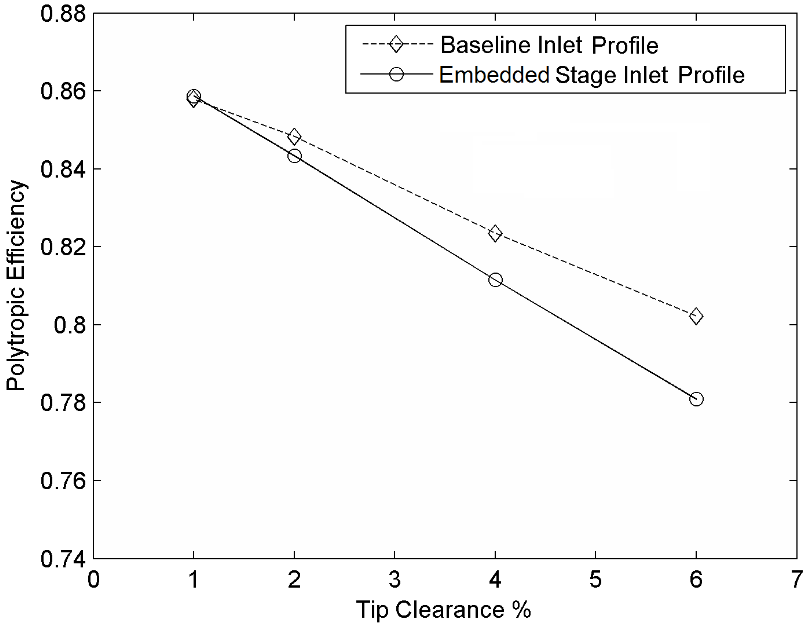

Figure 4-10: Polytropic efficiency versus tip clearance. Comparison of inlet velocity profiles. Efficiency calculated using mixed-out stagnation temperature and pressure as the outlet condition.

Re	200,000
Slope	-.0156
y intercept	.874
R^2	.999

Table 4.7: Linear regression results for tip clearance data. Embedded stage inlet velocity profile.

4.3.2 Efficiency Sensitivity at Large Clearances

Mixing of the leakage and free stream flows is the largest source of loss associated with tip clearances and provides the foundation for the loss estimation given in Equation 4.1 [5]. The results of Section 4.3.1 show that polytropic efficiency varies linearly with tip gap when a mixed-out condition is used as the outlet.

The spatial location of mixing is dependent on the tip clearance value. Figure 4-11 shows the change in non-dimensional entropy as a function of axial location for 2% and 6% tip clearances. Non-dimensional entropy is defined as

$$\Delta s_{non-dimensional} = \frac{\Delta s \, T_{02}}{h_0} \tag{4.17}$$

where Δs is the local change in entropy, T_{02} is the exit stagnation temperature, and h_0 is the local stagnation enthalpy. The x-axis in Figure 4-11 is axial location and the y-axis is non-dimensional entropy. Figure 4-11 illustrates that the entropy increase downstream of the trailing edge is larger for the 6% clearance than the 2% clearance.

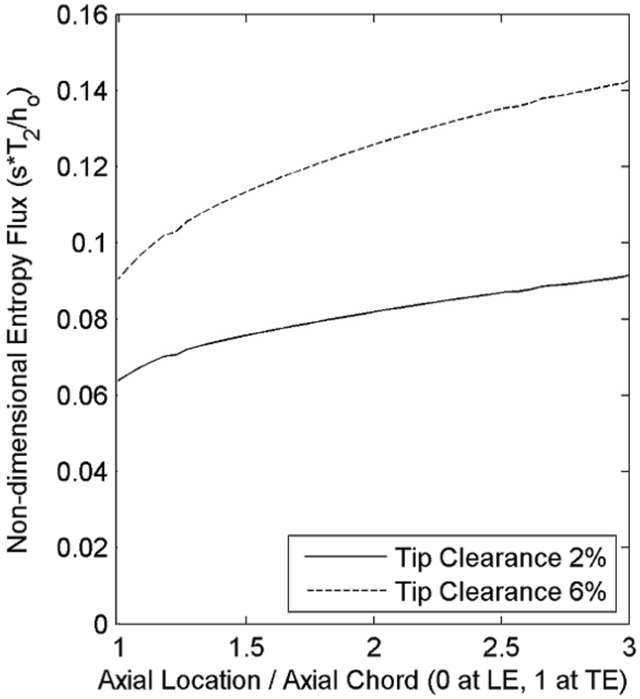

Figure 4-11: Entropy flux versus axial location (Re = 200,000).

This indicates that efficiency may not vary linearly with tip clearance in a full stage because at larger clearances, mixing occurs farther downstream. Sakulkaew found that for clearances greater than 3.4%, efficiency is less sensitive to tip clearance flow because the leakage flow moves towards the blade trailing edge and is unable to mix before leaving the rotor passage [25]. Figure 4-12 shows rotor efficiency as a function of tip clearance for an unsteady full-stage calculation, which illustrates how the efficiency penalty of clearances greater than 3.4% may be mitigated in a multi-stage compressor environment.

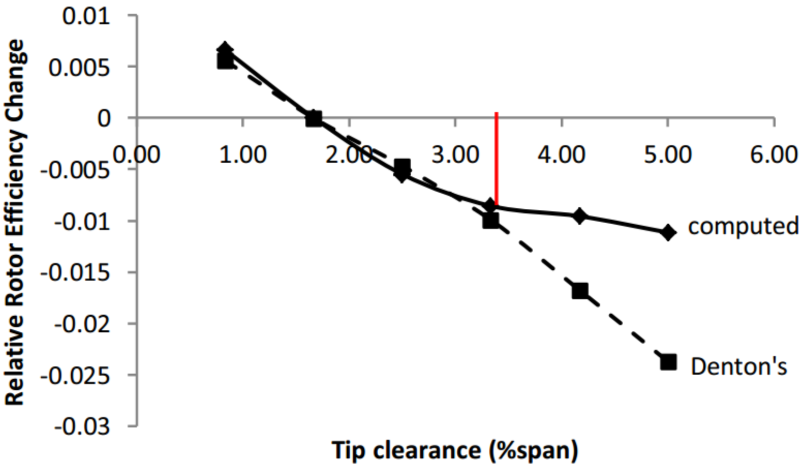

Figure 4-12: Rotor efficiency as a function of tip clearance for unsteady stage computations compared to Denton's clearance model. From Sakulkaew [25].

4.3.3 Compressor Size and the Impact of Tip Clearance

Using the clearance assumptions described in Section 4.1.1, the predicted tip clearance for the three compressor configurations and core sizes of 1.0 lbm/s to 6.0 lbm/s is given in Figure 4-13. The maximum efficiency penalty occurs at the stage with the largest non-dimensional clearance which, with these assumptions, is the last stage.

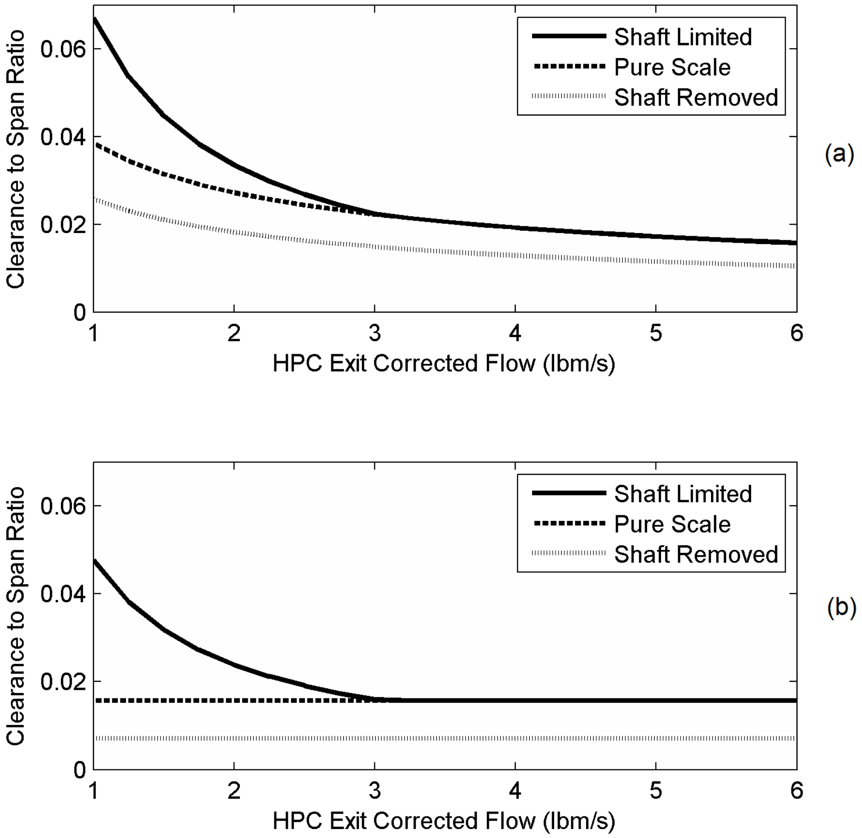

Figure 4-13: Maximum tip clearance based on core size and compressor configuration; (a) Clearances not scalable (b) clearances scalable.

Using the clearances of Figure 4-13 and the efficiency penalty results of Figure 4-10, the tip clearance efficiency penalty can be estimated for the three compressor configurations and for both clearance assumptions and Figures 4-14 and 4-15 show polytropic efficiency versus core size. In both Figures, the x-axis is HPC exit corrected flow and the y-axis is tip clearance efficiency penalty. The difference between the two figures is that Figure 4-14 uses the tip clearance results for a constant inlet velocity profile, whereas Figure 4-15 uses the results for the embedded stage inlet profiles. For this reason, the efficiencies shown in Figure 4-14 are quantitatively lower.

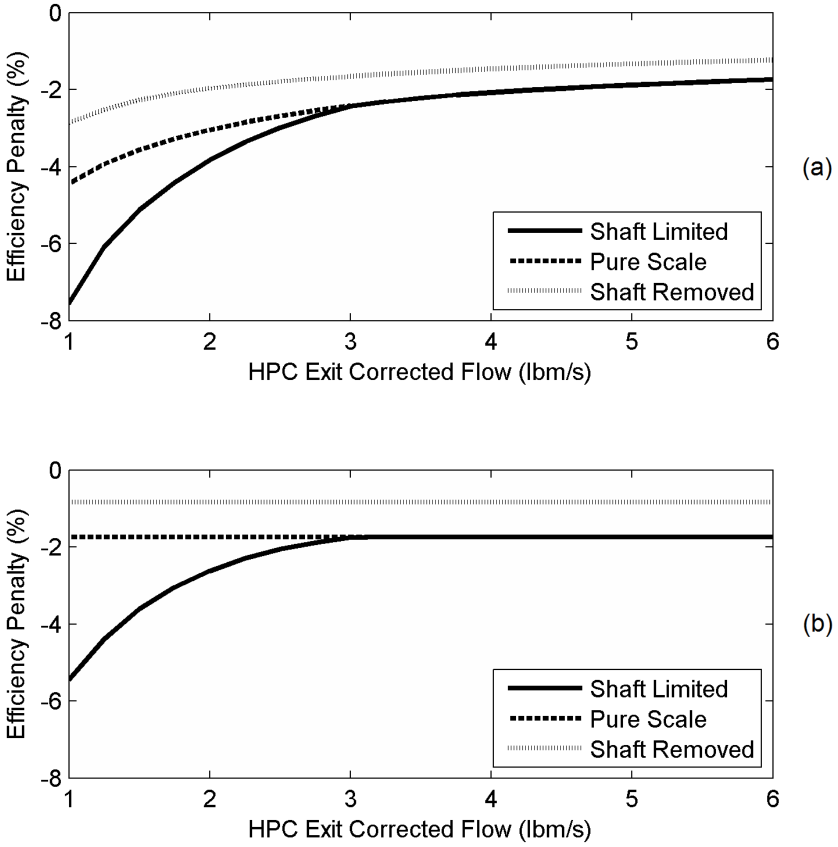

Figure 4-14: Last stage tip clearance rotor efficiency penalty for three configurations as a function of core size for baseline inlet velocity profile results: (a) Clearances not scalable (b) clearances scalable.

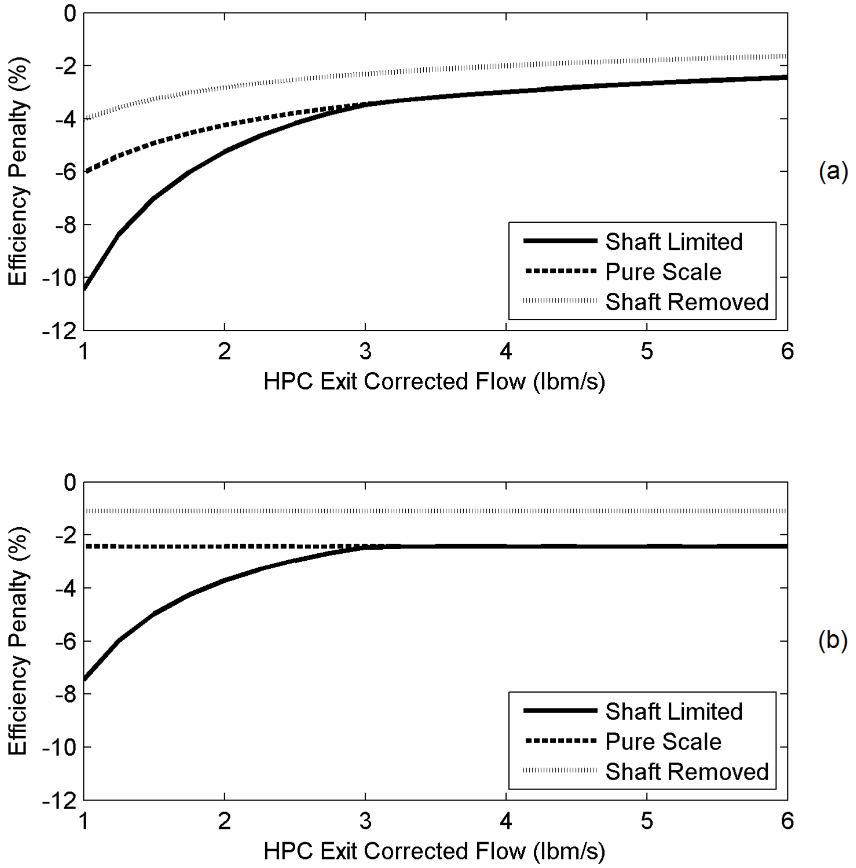

Figure 4-15: Last stage tip clearance rotor efficiency penalty for three compressor configurations as a function of core size for approximate embedded stage inlet velocity profiles: (a) Clearances not scalable (b) clearances scalable.

Both Figures 4-14 and 4-15, show the sensitivity of the tip clearance efficiency penalty to core size increases as core size is reduced. For example, assuming clearances not scalable, embedded stage velocity profiles, and a shaft limited configuration, there is a 1.0% drop in efficiency from a core size of 6.0 lbm/s to 3.0 lbm/s, and a much larger, 3.5%, drop in efficiency from a core size of 3.0 lbm/s to 1.5 lbm/s.

4.3.4 Tip Clearance Efficiency Penalty for a 1.5 lbm/s Core

For a core size of 1.5 lbm/s (the size of the D8.6 core) Table 4.8 summarizes the results from Figures 4-14 and 4-15 for this core size.

Inlet Condition	Scaling Assumption	Compressor Configuration		
		Shaft Limited	Pure Scale	Shaft Removed
Baseline Velocity Profile	Clearances Not Scalable	-5.1%	-3.6%	-2.3%
	Clearances Scalable	-3.6%	-1.7%	-0.8%
Embedded Stage Velocity Profile	Clearances Not Scalable	-7.0%	-4.9%	-3.3%
	Clearances Scalable	-5.0%	-2.4%	-1.1%

Table 4.8: Calculated tip clearance efficiency penalties for the last stage of a 1.5 lbm/s HPC.

From the results in Table 4.8, we can make quantitative statements about the impact of compressor configuration, tip clearance scaling, and inlet velocity profile on rotor efficiency penalty in the last stage of a 1.5 lbm/s core.

- Compressor Configuration - A shaft removed configuration is estimated to have a 2.8% - 3.9% efficiency benefit over a shaft limited configuration.
- Scaling Assumption - If clearances scale with compressor size, there is a 1.5%-2.5% increase in efficiency compared to if clearances do not scale with compressor size.
- Inlet Conditions - The embedded stage inlet condition reduces the calculated tip clearance efficiency by 0.3%-1.9%. The most substantial impact is for the shaft limited machine with its larger clearances.

These results are for the last stage of the HPC and therefore the efficiency penalties of an entire HPC will be less. The impact of tip clearances on an entire compressor will be discussed in Chapter 5.

4.3.5 Summary

Investigation of the effects of tip clearance for small core compressors has yielded the following:

1. For a shaft limited compressor configuration, if clearances are not scalable, a 4.5% tip clearance could exist for a 1.5 lbm/s core.
2. A shaft removed configuration decreases non-dimensional tip clearances even when clearances are not scalable because a reduction in mean radius leads to larger blade spans.
3. A 1.1% decrease in mixed-out polytropic efficiency was found for every 1% increase in tip clearance for an isolated rotor row with the inlet velocity profile held constant.
4. A 1.6% decrease in mixed-out polytropic efficiency was found for every 1% increase in tip clearance for an isolated rotor row with estimated embedded stage inlet conditions.
5. Tip clearance losses in a full stage may be less sensitive to gap-to-span ratio for clearances greater than 3.4% because the leakage and free stream flows mix farther downstream.
6. At a core size of 1.5 lbm/s, there may be a potential to reduce the tip clearance efficiency penalty by approximately 3%-4% (i.e. a potential to raise the stage efficiency) by using a shaft removed configuration rather than a shaft limited configuration.

Chapter 5

Methodology for Estimating the Effect of Core Size on Compressor Efficiency and Fuel Burn

5.1 Introduction

This chapter synthesizes the material presented in the previous four chapters by creating a methodology for estimating small core compressor efficiency.

1. HPC sizing is determined by the corrected flow at the HPC exit.
2. Based on compressor size and E^3 blade aspect ratios, Reynolds number is defined for all stages and the efficiency penalty of low Reynolds number operation is assessed based on Chapter 3.
3. Two tip clearance assumptions were made in Chapter 4, one that physical clearances do not scale and the other that physical tip clearances scale with compressor radius. Using these assumptions, the efficiency penalty due to tip clearance is assessed based on the findings of Chapter 4 for all compressor stages.
4. The polytropic efficiency of the entire HPC is determined using the stage-by-stage efficiency results. This differs from the work in previous chapters which

focused on the individual stage rather than the entire compressor.

5. PFEI fuel burn was found to determine the impact of compressor size and configuration on aircraft fuel burn.

Figure 5-1 gives a graphical outline of the steps in the efficiency estimation.

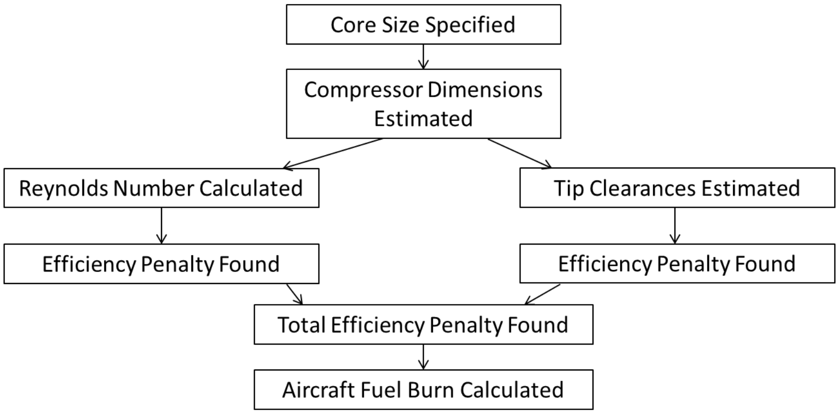

Figure 5-1: Small core engine fuel burn methodology.

5.2 Steps to Estimate Fuel Burn

5.2.1 Step 1: Determining HPC Size

The first step in estimating fuel burn is to size the high pressure compressor. Using the approach described in Appendix A, the geometry of each stage in the HPC can be determined for a given corrected flow and compressor configuration. For this thesis, the design space was defined as core sizes between 1.0 lbm/s to 6.0 lbm/s and as the three aforementioned compressor configurations. Figure 5-2 shows blade height as a function of compressor stage for the pure scale configuration. Table 3.1 gives a stage by stage summary of the assumed HPC.

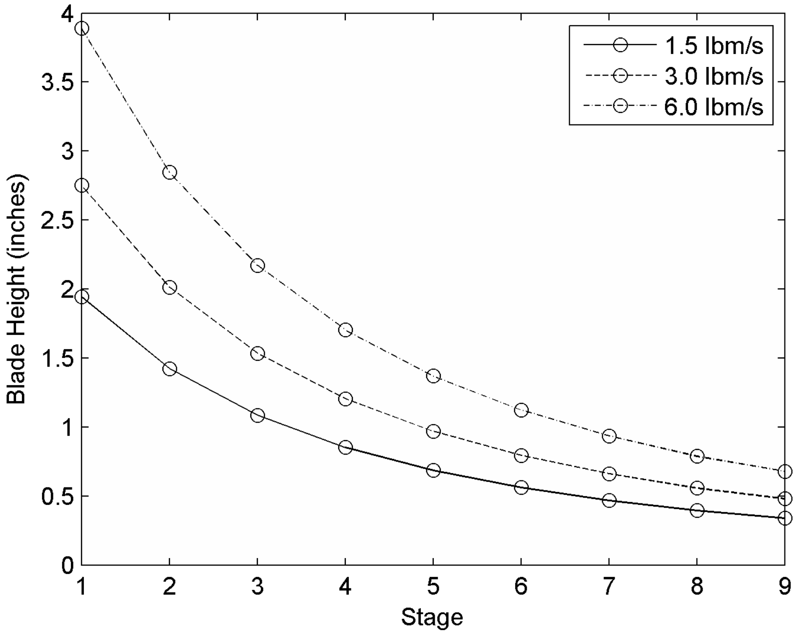

Figure 5-2: Rotor height versus stage for corrected flows of 1.0 - 6.0 lbm/s (pure scale configuration).

5.2.2 Step 2: Assessing Reynolds Number Effects

Using the operating conditions described in Appendix A, the Reynolds number for each stage was computed and the adiabatic efficiency penalty was calculated for each stage assuming a baseline stage with $Re = 500,000$ and E^3 blading. The adiabatic efficiency was then converted to polytropic efficiency using the stage pressure ratio as in Equation 5.1.

$$\eta_{poly} = \frac{\left(\frac{\gamma-1}{\gamma}\right)\ln\left(\frac{P_{out}}{P_{in}}\right)}{\ln\left(\frac{\left(\frac{P_{out}}{P_{in}}\right)^{\frac{\gamma-1}{\gamma}}-1+\eta_{adia}}{\eta_{adia}}\right)} \tag{5.1}$$

Figure 5-3 shows the stage polytropic efficiency penalty due to Reynolds number effects as a function of stage in a pure scale HPC. The x-axis is compressor stage and the y-axis is stage polytropic efficiency penalty compared to a stage with a rotor Reynolds number of 500,000.

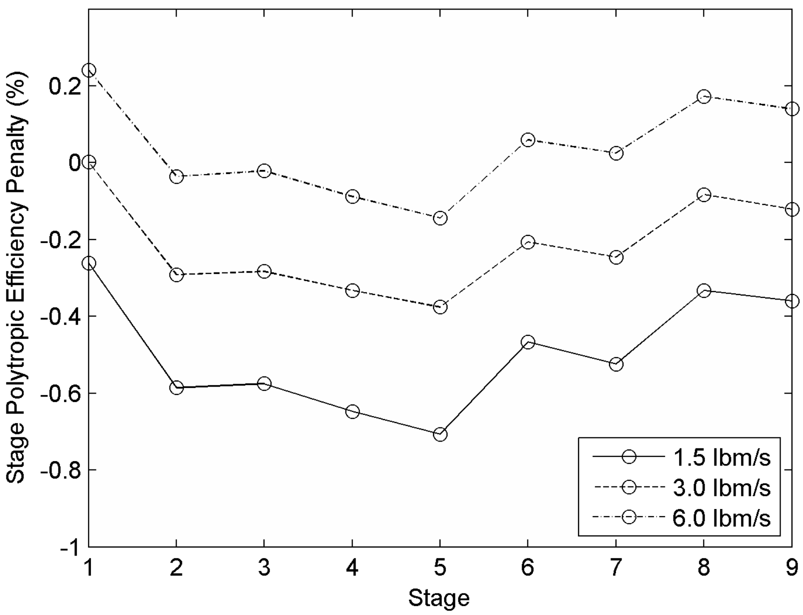

Figure 5-3: Reynolds number efficiency penalty by stage through the compressor. Core sizes indicated in legend. Baseline Reynolds number 500,000. Pure scale configuration displayed.

5.2.3 Step 3: Assessing Tip Clearance Losses by Stage

The HPC tip clearances were calculated using the two assumptions described in Section 4.1.2: constant physical clearance and scaling with radius. Using these tip clearances, the polytropic efficiency penalties were determined based on Figure 4-10. Stator hub clearances were not included.

To illustrate how tip clearance impacts polytropic efficiency through a compressor, Figure 5-4 gives tip clearance efficiency penalty versus stage for the pure scale compressor configuration using the constant physical clearance assumption. The x-axis is compressor stage and the y-axis is the polytropic efficiency penalty associated with tip clearance.

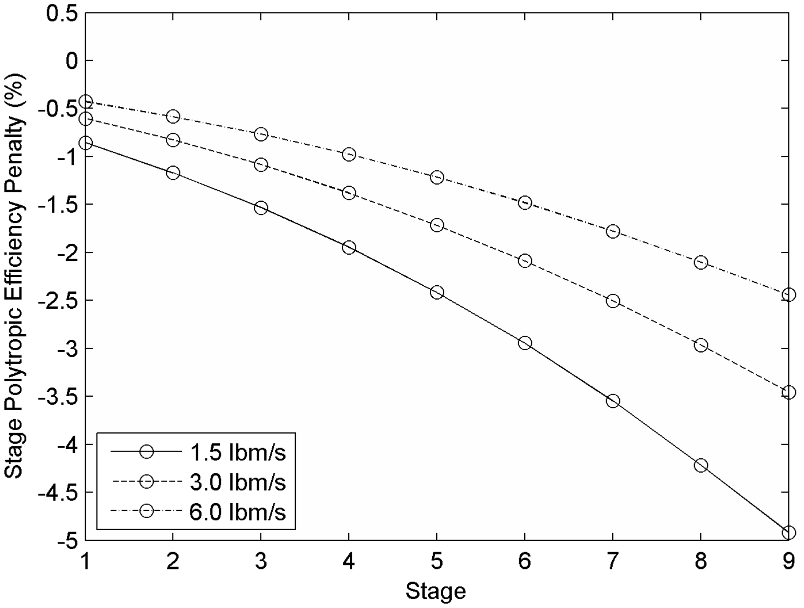

Figure 5-4: Tip clearance efficiency penalty for each stage in a pure scale configuration. Constant physical clearance assumed.

5.2.4 Step 4: Estimating HPC Efficiency

From Steps 2 and 3, we can find the entire HPC efficiency for different compressors. The efficiency is dependent on the assumptions made, and, to bound the problem, we define two limiting cases.

1. Case A - This represents an estimated upper bound to compressor efficiency. The assumptions for Case A are: a) Blade optimization to mitigate Reynolds number effects. b) Tip clearances scale with compressor radius.

2. Case B - This represents an estimated lower bound to compressor efficiency. The assumptions for Case B are: a) Blade optimization for Reynolds number not used. b) Tip clearances not scalable.

The calculated efficiency assumes that only Reynolds number and tip clearance losses will change in a small core HPC. The baseline HPC is at a core size of 6.0 lbm/s.

Figure 5-5 shows the entire HPC efficiency versus core size for Case A and Figure 5-6 does the same for Case B. Table 5.1 gives estimated efficiencies for Case A and Case B for all three configurations at a core size of 1.5 lbm/s. The efficiency penalty of Case B is 30%-40% greater than Case A.

A stronger effect, however, is that of configuration and Table 5.1 shows the importance of compressor configuration on compressor efficiency. There is a 4.1%-5.4% efficiency penalty for a 1.5 lbm/s core using the shaft limited configuration, but a 0.7%-1.0% efficiency penalty for a shaft limited case. This illustrates the potential efficiency benefit associated with reducing the mean radius of a small core compressor.

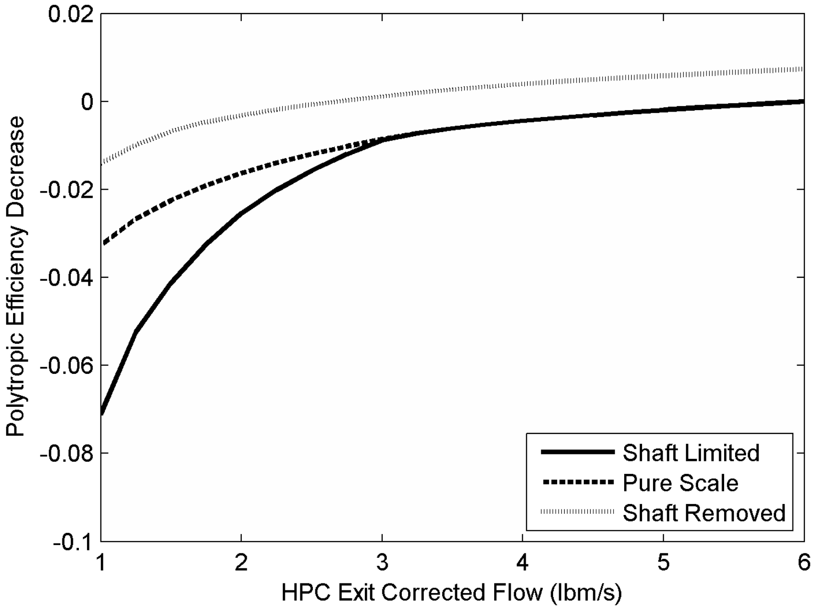

Figure 5-5: HPC efficiency versus core size for Case A (efficiency upper bound). Baseline efficiency at 6.0 lbm/s.

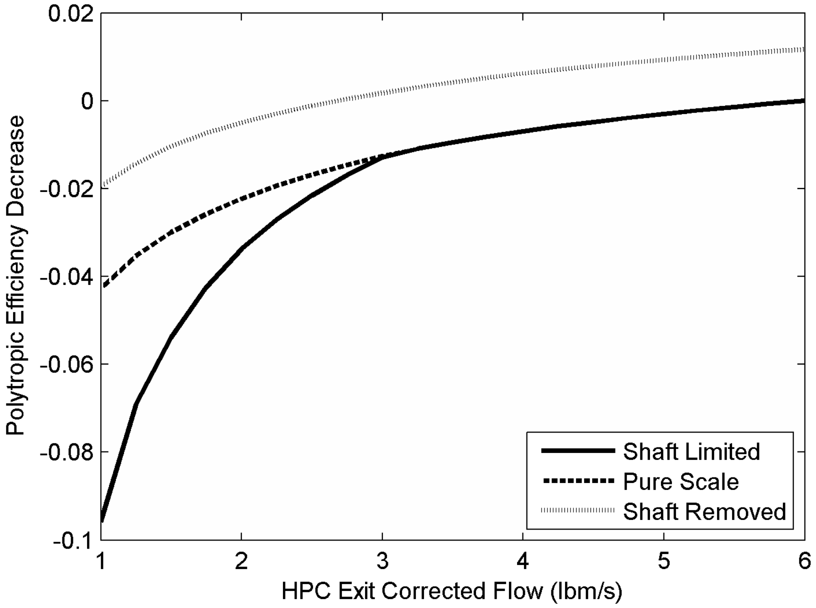

Figure 5-6: HPC efficiency versus core size for Case B (efficiency lower bound). Baseline efficiency at 6.0 lbm/s.

Case	Compressor Configuration		
	Shaft Limited	Pure Scale	Shaft Removed
Case A: HPC Efficiency Upper Bound	-4.1%	-2.2%	-0.7%
Case B: HPC Efficiency Lower Bound	-5.4%	-3.0%	-1.0%

Table 5.1: Efficiency penalties for a 1.5 lbm/s HPC compared to a 6.0 lbm/s HPC. Case A and Case B compared.

5.2.5 Step 5: Fuel Burn Impact

Using the results found in Table 5-7, TASOPT was employed to calculate the minimum fuel burn for the three configurations and the two cases (Case A and Case B). Figure 5-7 is a reproduction of Figure 2-8 with the efficiencies of the three configurations and two cases indicated. The D8.6 “baseline” HPC efficiency is 90%. Table 5.2 summaries the performance of the D8.6 aircraft with a 1.5 lbm/s HPC.

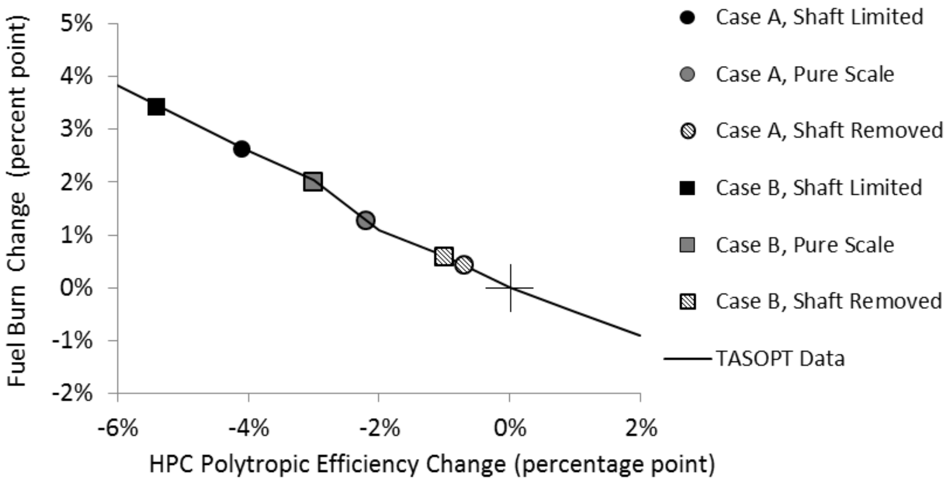

Figure 5-7: D8.6 fuel burn change versus HPC efficiency change. Three different compressor configurations and both cases (Case A: HPC efficiency upper bound, Case B: HPC efficiency lower bound) shown.

Case	Configuration		
	Shaft Limited	Pure Scale	Shaft Removed
Case A: HPC Efficiency Upper Bound	+2.6%	+1.3%	+0.4%
Case B: HPC Efficiency Lower Bound	+3.4%	+2.0%	+0.6%

Table 5.2: Fuel burn change for the D8.6 aircraft with a 1.5 lbm/s HPC.

There is a 0.4%-0.6% increase in fuel burn for the shaft removed configuration because HPC polytropic efficiency is reduced by 0.7%-1.0%. The fuel burn penalty increases to 1.3%-2.0% for the pure scale configuration. The shaft limited configuration has the largest penalty of 2.6%-3.4%, as HPC efficiency is reduced by as much as 5.4%.

These results indicate there is a fuel burn penalty associated with compressor inefficiencies in a small core engine, regardless of design. Perhaps the most important result, however, is that the impact of compressor size on fuel burn is highly dependent on the configuration chosen. With a shaft removed configuration, fuel burn can be reduced by 2.2%-2.8% compared to a shaft limited configuration.

Chapter 6

Summary, Conclusions, and Suggestions for Future Work

Small core jet engines are a focus in the aircraft engine industry as they are both a byproduct of, and a necessity for, efficient jet engine cycles for advance single-aisle aircraft. Two major sources of inefficiency in the compressors of small core engines, low Reynolds numbers and large tip clearance, have been computationally assessed. Three different compressor configurations were examined to estimate the efficiency penalty associated with each when operated at flows as low as 1.5 lbm/s. The impact of compressor size, blade geometry, tip clearance, and compressor configuration have been assessed against a global metric, aircraft mission fuel burn.

6.1 Summary and Conclusions

1. Three types of small core compressor configurations were examined for a 1.5 lbm/s core size. One was a direct scaling from current compressors for single-aisle civil transport aircraft. A second was a configuration in which the minimum radius was set at a value that is consistent with an existing small core engine low pressure spool shaft diameter. The third configuration allowed the minimum radius to be pulled in, so the hub/tip radius ratio of the last stage could decrease. Blade size, Reynolds number, and tip clearance were all found to

be dependent on configuration, with the shaft limited configuration presenting the greatest challenge (lowest Reynolds numbers and largest tip clearances).

2. The lowest rotor Reynolds numbers expected for the 1.5 lbm/s shaft limited compressor is 160,000. This had a 2.3% decrease in stage efficiency compared to $Re = 1.1 \times 10^6$ operation.

3. Blade and vane geometry optimization can mitigate the effects of low Reynolds number in the shaft limited configuration. For the shaft limited compressor examined, the efficiency increase from an optimized blade was 0.2% for the entire compressor. Blade optimization can have a larger impact at Reynolds numbers below 150,000, i.e., for core sizes below 1.5 lbm/s.

4. To bound the examination of the effects of clearance, two limiting cases were examined. The first was fixed clearance, i.e., clearance held at a value representative of single-aisle aircraft engine high compressors. The second was based on the ability to scale clearances with radius. If clearances are fixed (i.e., do not scale with core size), the maximum tip clearance in a 1.5 lbm/s HPC could be 4.5%, leading to a stage efficiency penalty of 7.0%.

5. The fuel burn increase associated with small core compressor inefficiency is between 0.4% and 3.4%, depending on compressor configuration and tip clearance scaling.

6. Decreasing the mean radius of a machine allows blades to become larger in size so so that Reynolds numbers are maximized and tip clearances are minimized. This can be achieved by pulling in the flow path. An example in which the rear stage hub-to-tip ratio was reduced from 0.93 to 0.85 indicated that compressor polytropic efficiency increases by 1.5%-2.0% for a 1.5 lbm/s core.

7. Tip clearances are the largest source of inefficiency in a small core compressor, regardless of configuration. Chapter 4 shows approximately a 1.6% gain in efficiency for every 1% reduction in gap-to-span ratio. If physical tip clearances

can be scaled, there is a 1.5-2.5% increase in efficiency, for the compressor studied, compared to the case in which clearances do not scale.

6.2 Suggestions for Future Work

6.2.1 Ultimate Steady Flow at Different Tip Clearances

Chapter 4 presented an approximate analysis of tip clearance losses in an embedded stage of a multistage compressor. This shows a steeper falloff in efficiency with increased tip clearance than for an isolated rotor at the same clearance. For this estimate, the inlet velocity profile was found from Smith's [27] displacement thickness approximation and a tangential velocity that was assumed to have the same flow angle, regardless of tip clearance. Because of the high impact of tip clearance, and the fact that much of the tip clearance literature is for isolated blade rows, it is important to examine tip clearance flow in multistage compressors at clearances characteristic of small cores, both for performance values and for flow features and loss mechanisms. Multistage computations coupled with experimental work in a multistage rig would both be of considerable worth.

As an example of one of the unknowns, the efficiency penalties calculated in Chapter 4 were found using the fully mixed-out state downstream of the rotor row. However, the flow does not completely mix before entering the downstream stator, with the amount of mixing increasing as tip clearance increases. A recent finding is that because of this, the efficiency does not decrease with tip clearance as strongly above clearances of about 3.5% as below this value, although this computational result is only over a limited geometry range [25]. Future work to determine the generality of such effects would thus be valuable.

An issue not addressed in this thesis was the effect of compressor size on blade geometry. For example, for structural and other reasons, compressor blades must meet certain minimum thickness requirements. The airfoil shape of a small core blade may need to be thicker than aerodynamically desired or the leading edge radius may become blunt and lead to higher losses. Perhaps more importantly, however, as blade size decreases, it becomes more difficult to achieve the geometry that has been designed. The impact of manufacturing processes on performance is an aspect we did not address, and this is still a large unknown in the problem. Another important next step is thus quantification of these effects and definition of avenues to address them. As above, this should not only involve computations, but also experiments, because the questions need to be answered in the context of the multistage environment.

A final comment is that although this is a component issue, the engine configuration will again play a role; a shaft removed design, with its larger blades, will be less susceptible than a shaft limited design, and the ability to make the trade between configuration and component attributes and performance is a necessary piece of designing for small core engines of the future.

Appendix A

Reynolds Number Calculations for the D8.6 HPC

Changes in Flow Properties Due to Compression

Using the D8.6 flight conditions (Po2, To2), the flow properties through the entire compression process can be understood (fan, booster, and HPC). Assumptions are as follows:

- Axial Mach number of 0.58 at compressor entrance.
- Constant axial velocity of 170 m/s.
- Polytropic efficiency of 90% through each stage.

Fluid properties at the compressor exit are plotted as a function of pressure ratio and polytropic efficiency in Figures A-1, A-2, and A-3. The key findings include:

- Density increases, flow area decreases.
- Dynamic viscosity increases (almost purely a function of temperature, see Figure A-5).
- Kinematic viscosity decreases (density increases more than dynamic viscosity increases).

$$\upsilon = \frac{\mu}{\rho} \tag{A.1}$$

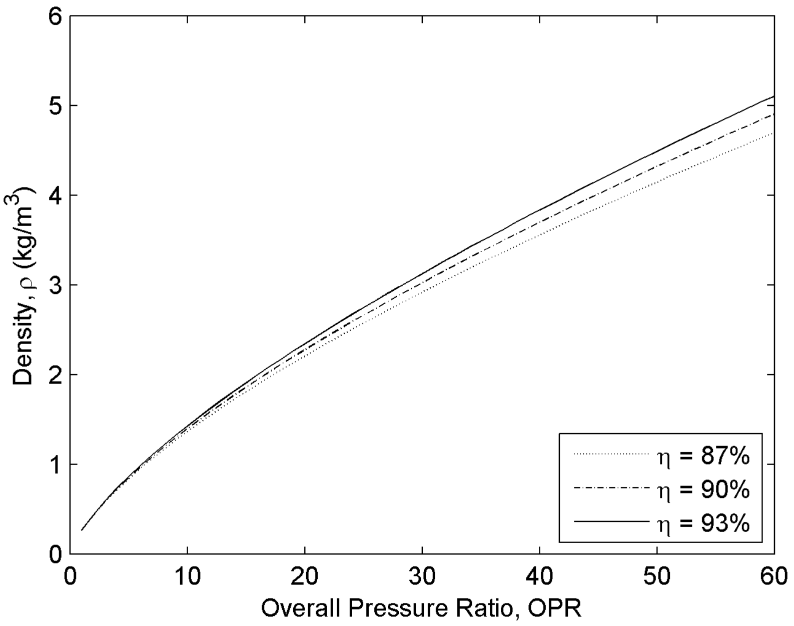

Figure A-1: Exit density versus OPR for a compressor.

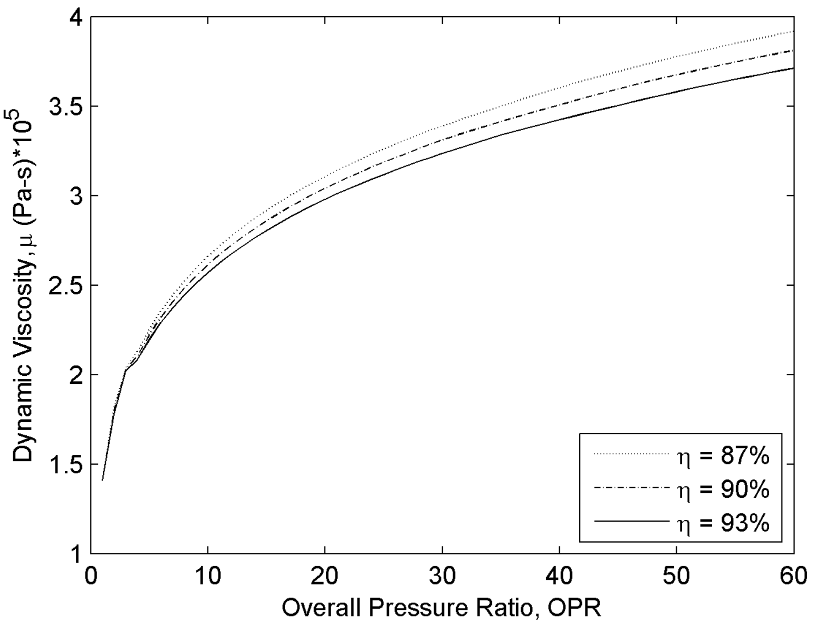

Figure A-2: Exit dynamic viscosity versus OPR for a compressor.

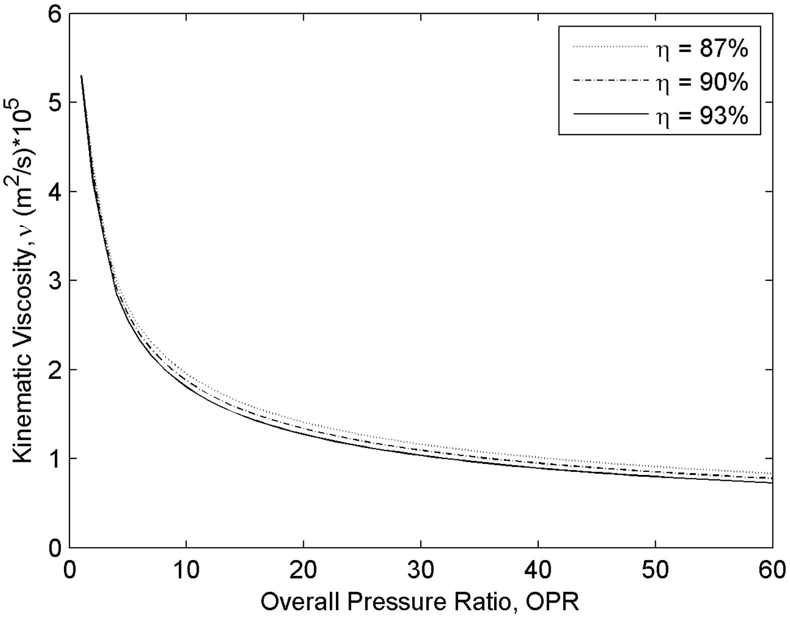

Figure A-3: Exit Kinematic Viscosity versus OPR for a compressor.

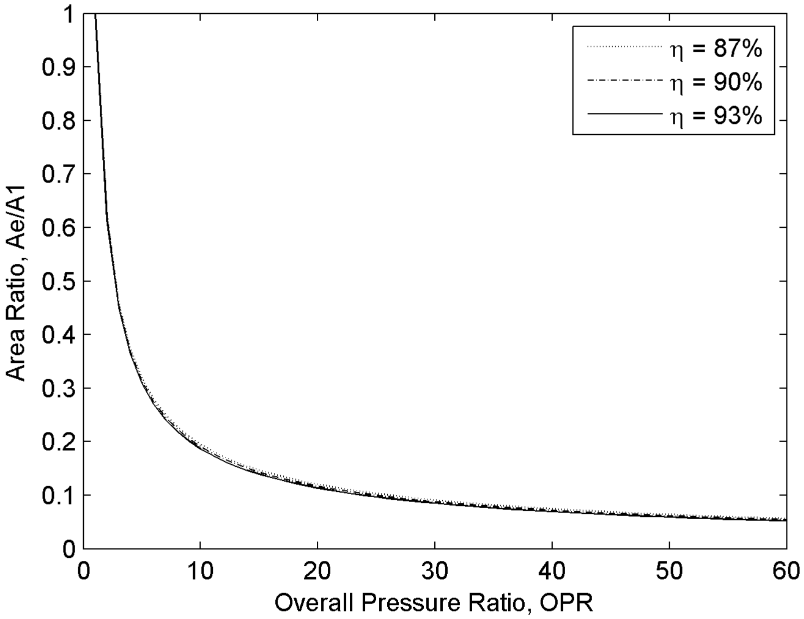

Figure A-4: Exit flow area versus OPR.

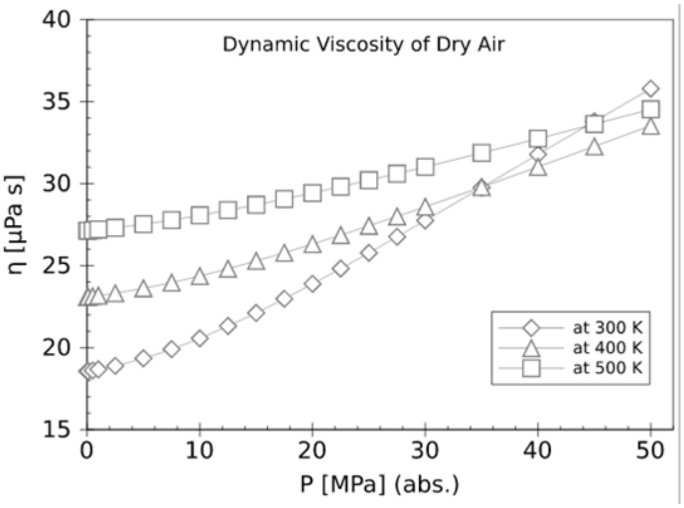

Figure A-5: Dynamic viscosity of air as a function of pressure. Note that viscosity is much more dependent on temperature than pressure for pressures less than 2 MPa.

Calculations for the D8.6 HPC

We can find the flow properties at the entrance of the high pressure compressor using the cycle analysis program GasTurb. All efficiencies used are those listed in Table 2.1. The HPC entrance conditions are:

- Po= 47.13 kPa
- To = 308.6 K
- ρ=0.4709 kg/m3
- $\dot{\text{m}}$=4.100 kg/s

In the previous sections, it was found that kinematic viscosity and flow area both decrease through the compressor. These effects compete with one another in the Reynolds number equation, A.2.

$$Re = Vc/\nu \tag{A.2}$$

It is not entirely clear at first glance how the Reynolds number will vary through the HPC. To calculate Reynolds number compressor assumptions are listed in Table A.1.

HPC Entrance Mach Number	0.5
Axial Velocity (constant)	170 m/s
Flow Coefficient, ϕ	0.50
IGV Angle	20 degrees
Polytropic Efficiency	0.90
Mean Radius	0.15 m

Table A.1: D8.6 HPC compressor assumptions.

For these calculations, the compressor configuration was assumed to be shaft limited. The mean radius of the compressor was estimated using the PW308 as a reference. Using the PW308 HPC mean radius, the radius of the D8.6 HPC was approximated to be 0.15m [12]. This value was held constant through the machine.

Plots of flow area, blade height, and Reynolds number as a function of HPC pressure ratio are shown in Figures A-6, A-7, and A-8. The plot of Reynolds number versus HPC pressure ratio also shows the impact of blade aspect ratio. For constant aspect ratio, the Reynolds number decreases through the HPC.

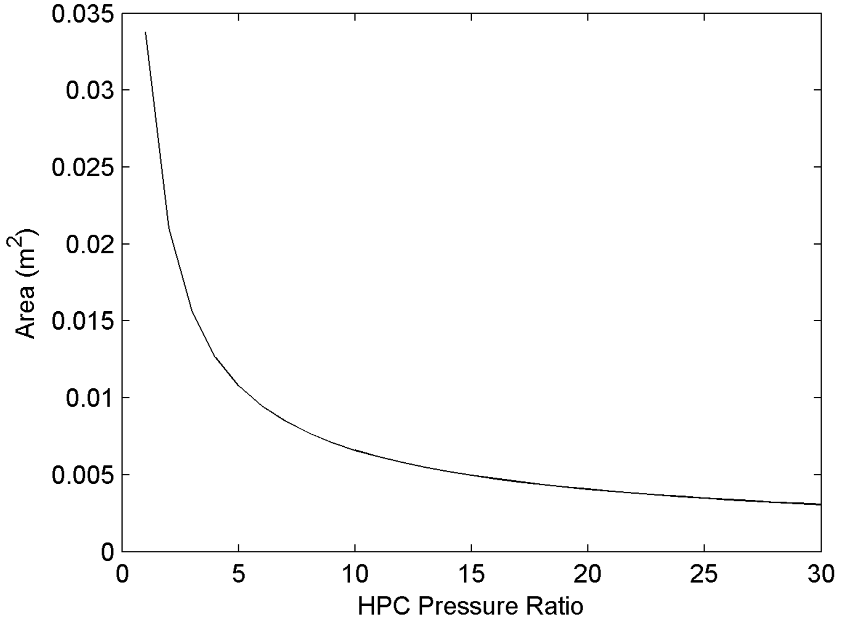

Figure A-6: Flow area versus HPC pressure ratio.

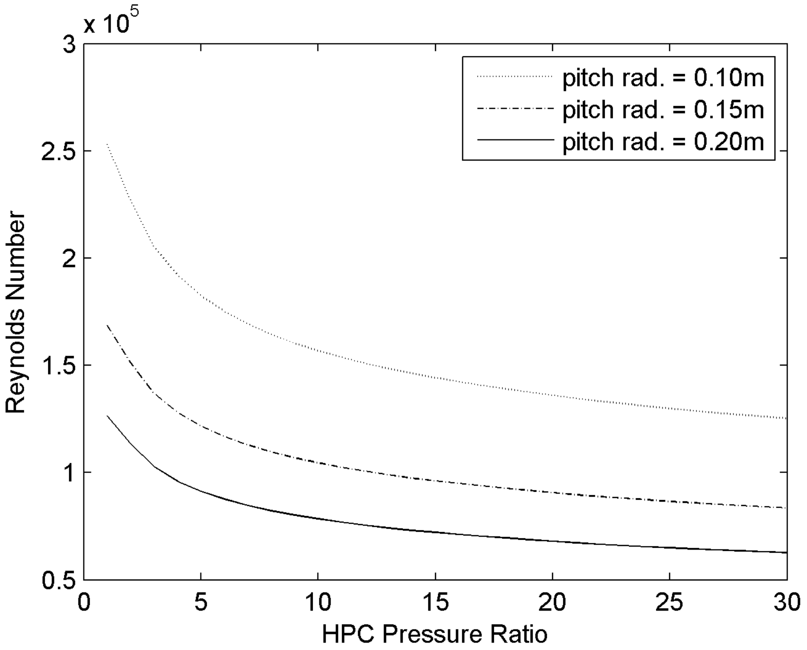

Figure A-7: Rotor Reynolds number versus HPC pressure ratio.

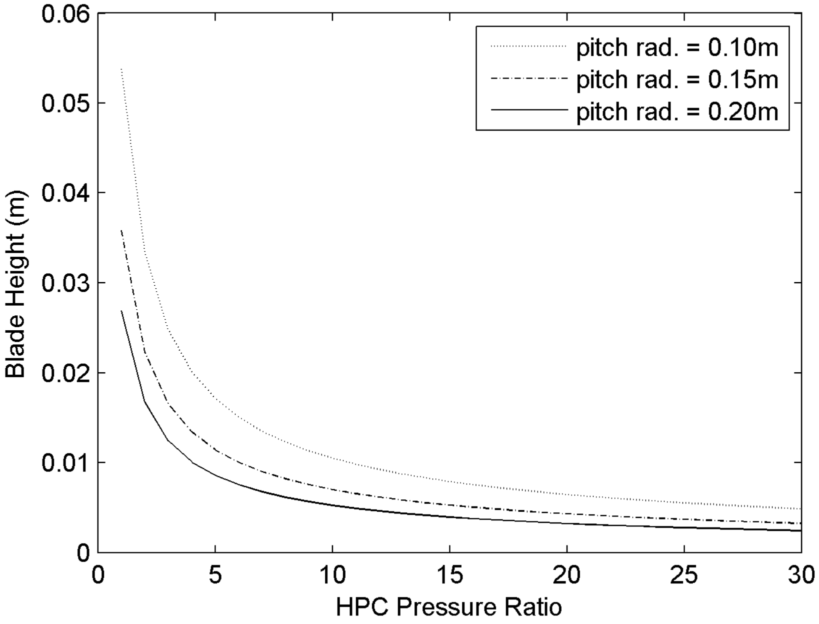

Figure A-8: Blade height versus HPC pressure ratio.

In a typical compressor, however, the blade aspect ratios change from front to rear of the machine. To calculate D8.6 Reynolds numbers, the aspect ratios of the E^3 compressor were used. These aspect ratios are listed in Table A.2 and were estimated from cross-sections given in Jane's Aeroengines [12].

Stage #	1	2	3	4	5	6	7	8	9
Aspect Ratio	1.5	2.0	1.8	1.8	1.8	1.3	1.3	1.0	1.0

Table A.2: Aspect ratios of the E^3 compressor [12].

The stages of the D8.6 compressor were assumed to be evenly loaded (same Δh_0). The final plot of Reynolds number versus HPC stage is found in Figure 3-2. Note that the lowest Reynolds numbers are near the front/middle of the machine, not in the rear stages. The lowest value encountered is approximately 160,000.

Appendix B

Efficiency Estimates for Cascade Results

Adiabatic efficiency can be approximated using the entropy generated and the enthalpy rise of the compressor process [5].

$$\eta_{adiabatic} \approxeq 1 - \frac{T_2 \Delta s}{\Delta h_0} \tag{B.1}$$

Assuming adiabatic flow through the blade row, entropy generation is given by:

$$\Delta s = -R \ln \left(\frac{P_{02}}{P_{01}} \right) \tag{B.2}$$

Substituting MISES output parameters:

$$\Delta s = -R \ln \left(1 - \omega \left(1 - \frac{P_1}{P_{01}} \right) \right) \tag{B.3}$$

Equation B.3 is applicable for both the rotor and stator rows in their relative reference frames as entropy is a state quantity and is independent of reference frame.

The enthalpy rise of the stage can be found using Euler's work equation in the relative frame:

$$\Delta h_0 = U V_x \left(\tan \alpha_1^{rel} - \tan \alpha_2^{rel} \right) \tag{B.4}$$

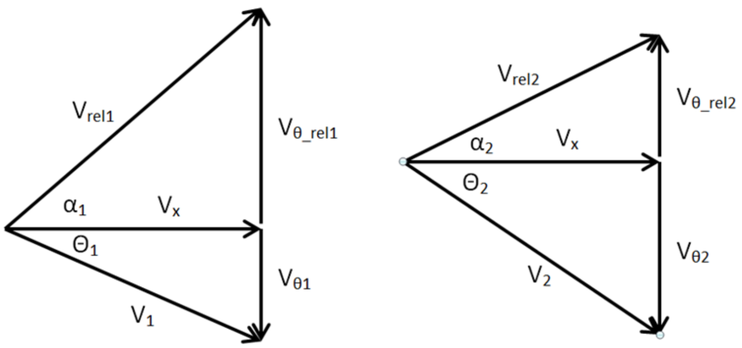

Figure B-1: Velocity triangles at rotor inlet (left) and exit (right).

With some algebraic manipulation, enthalpy can be calculated using MISES inputs and outputs.

$$\Delta h_0 = \gamma R T_1 M^2 \cos\alpha_1 \left(\sin\alpha_1 + \cos\alpha_1 \tan\alpha_1\right)\left(\tan\alpha_1 - \tan\alpha_2\right) \tag{B.5}$$

Appendix C

References

Casing Radius	60.96 cm
Hub Radius	48.8 cm
Hub-to-tip ratio	0.80
Blade Span	12.19 cm
Rotational Speed	958 rpm
Rotor tip speed (based on casing radius)	61.15 m/s
Mass Flow	12.3 kg/s
Axial Velocity	24.4 m/s
Pressure Ratio	1.042
Temperature Ratio	1.013
Flow Coefficient, ϕ	0.400
Average Pressure Rise Coefficient	0.500
Number of Rotor Blades	39
Number of Stator Vanes	52
Mid-span Aerodynamic Chord (rotor)	10.2 cm
Mid-span Aerodynamic Chord (stator)	9.4 cm

Table C.1: Baseline parameters for the NASA Large Low-Speed Axial-Flow Compressor [29].

Bibliography

[1] Becker, A.C., et al. N+3 discussion between MIT and Pratt and Whitney, Pratt and Whitney, East Hartford, CT, 31 July 2012.

[2] Carter, A. D. S., "The Effect of Reynolds Number on the Performance of a Single-Stage Compressor," Aeronautical Research Council Reports and Memoranda, Ministry of Aviation, No. 3184, May 1957.

[3] Cumpsty, N. A., *Jet Propulsion: A Simple Guide to the Aerodynamic and Thermodynamic Design and Performance of Jet Engines*, *2nd ed.*, Cambridge University Press, 2003.

[4] Cumpsty, N. A., *Compressor Aerodynamics, 1st ed.,* Longman Group UK Ltd., 1989.

[5] Denton, J. D., "Loss Mechanisms in Turbomachines - The 1993 IGTI Scholar Lecture," *Journal of Turbomachinery*, Vol. 115, pp. 621-656, Oct. 1993.

[6] Drela, M. "Low-Reynolds-Number Airfoil Design for the M.I.T. Daedalus Prototype: A Case Study." *Journal of Aircraft*. Vol. 25, No. 8, 1988.

[7] Drela, M. et al. "N+3 Aircraft Concept Designs and Trade Studies, Final Report, Volume 2: Appendices – Design Methodologies for Aerodynamics, Structures, Weight, and Thermodynamic Cycle." Technical Report. NASA CR-2010-216794/VOL2, NASA, 2010.

[8] Drela M., and Giles, M. B. "Viscous-inviscid Analysis of Transonic and Low Reynolds Number Airfoils". AIAA Journal, 25(10):1347–1355, Oct. 1987.

[9] Freeman, C. *Effect of Tip Clearance Flow on Compressor Stability and Engine Performance.* von Karman Institute for Fluid Dynamics, Lecture Series 1985-05, 1985.

[10] Greitzer, E. M., et. al. "N+3 Aircraft Concept Designs and Trade Studies." Technical Report. NASA CR-2010-216794, NASA, 2010.

[11] Greitzer, E.M., Tan, C. S., and Graf, M.B. *Internal Flow.* Cambridge University Press, 2004.

[12] Gunston, B. (ed.). J*ane's Aero-Engines, Iss. 27*, ed. Daly, M., Odyssey Press, Mar. 2010.

[13] Gupta, A., Khalid, S. A., McNulty, G. Scott, and Dailey, L. "Prediction of Low Speed Compressor Rotor Flowfields with Large Tip Clearances," *ASME/IGTI Turbo Expo 2003*, Jun. 2003.

[14] Guynn, M. D., et al. *Refined Exploration of Turbofan Design Options for an Advanced Single-Aisle Transport.* Technical Report. NASA/TM–2011-216883. Jan. 2011.

[15] Hall, D. K. *Performance Limits of Axial Turbomachinery Stages.* Master's Thesis. MIT. Dec. 2010

[16] Hathaway, M.D. E-mail to Austin DiOrio, 22 Aug. 2012.

[17] Henne*,* P.A. (ed.). *Applied Computational Aerodynamics, Vol. 125.* 1990.

[18] Howard, M. A., Ivey, P. C., Barton, J. P., and Young, K. F. "Endwall Effects at Two Tip Clearances in a Multistage Axial Flow Compressor with Controlled Diffusion Blading." *Journal of Turbomachinery.* Vol. 116, pp. 635-645, Oct. 1994.

[19] Howell, A. R. "Fluid Dynamics of Axial Compressors." *War Emergency Proc. No. 12 Inst. Mech. Engrs.* Appendix II, pp. 451-452. Jan. 1957.

[20] Hunter, I. H. and Cumpsty, N. A. "Casing Wall Boundary-Layer Development Through and Isolated Compressor Rotor," *Journal of Engineering for Power*, Vol. 104 Iss. 4, pp. 805-817, Oct. 1982.

[21] Koch, C. C., Smith, L. H., "Loss Sources and Magnitudes in Axial-Flow Compressors," *Journal of Propulsion and Power*, Vol. 20, No. 4, pp. 557-595, Aug. 2004.

[22] Mellor, G. L. and Strong, R. E. "End-wall Effects in Axial Compressors". *ASME paper No. 67-FE-16*, May 1967.

[23] NUMECA International. "FINE User Manual, Version 6.2-d." May 2005.

[24] Roberts, W. B., "The Effect of Reynolds Number and Laminar Separation on Axial Cascade Performance," *Journal of Engineering for Power*, Vol. 97, Iss. 2, pp. 261-273, April 1975.

[25] Sakulkaew, S., Tan, C.S., Donahoo, E., Cornelius, E., and Montgomery, M. "Compressor Efficiency Variation with Rotor Tip Gap from Vanishing to Large Clearance." *ASME Turbo Expo 2012,* GT2012-68367, June 2012.

[26] Schaffler, A., "Experimental and Analytical Investigation of the Effects of Reynolds Number and Blade Surface Roughness on Multistage Axial Flow Compressors." *Journal of Engineering for Power*. Ser. A, Vol. 102, pp. 5-13. 1980.

[27] Smith, L. H. "Casing Boundary Layers in Multistage Axial-Flow Compressors". *Proceeding of the Symposium on Flow Research on Blading, BBC Limited, Switzerland*. pp. 275-304. 1969.

[28] Sonoda, T., et. al. "Advanced High Turning Compressor Airfoils for Low Reynolds Number Condition— Part I: Design and Optimization." *Journal of Turbomachinery*. Vol. 126, pp. 350-359, July 2004.

[29] Wellborn, S. R., and Okiishi, T. H., "Effect of Shrouded Stator Cavity Flows on Multistage Axial Compressor Aerodynamic Performance", NASA Contractor Report 198536, Oct. 1996.